The North Atlantic Waveguide and Downstream Impact Experiment

Andreas Schäfler, George Craig, Heini Wernli, Philippe Arbogast, James D. Doyle, Ron McTaggart-Cowan, John Methven, Gwendal Rivière, Felix Ament, Maxi Boettcher, Martina Bramberger, Quitterie Cazenave, Richard Cotton, Susanne Crewell, Julien Delanoë, Andreas Dörnbrack, André Ehrlich, Florian Ewald, Andreas Fix, Christian M. Grams, Suzanne L. Gray, Hans Grob, Silke Groß, Martin Hagen, Ben Harvey, Lutz Hirsch, Marek Jacob, Tobias Kölling, Heike Konow, Christian Lemmerz, Oliver Lux, Linus Magnusson, Bernhard Mayer, Mario Mech, Richard Moore, Jacques Pelon, Julian Quinting, Stephan Rahm, Markus Rapp, Marc Rautenhaus, Oliver Reitebuch, Carolyn A. Reynolds, Harald Sodemann, Thomas Spengler, Geraint Vaughan, Manfred Wendisch, Martin Wirth, Benjamin Witschas, Kevin Wolf, Tobias Zinner

Affiliations: SCHÄFLER, BRAMBERGER, DÖRNBRACK, EWALD, FIX, GROß, HAGEN, LEMMERZ, LUX, RAHM, RAPP, REITEBUCH, WIRTH AND WITSCHAS — Deutsches Zentrum für Luft- und Raumfahrt, Oberpfaffenhofen, Germany; CRAIG, GROB, KÖLLING, MAYER AND ZINNER — Ludwig-Maximilians-Universität, München, Germany; BOETTCHER, GRAMS AND WERNLI — ETH Zürich, Switzerland; ARBOGAST — Météo-France/CNRS, Toulouse, France; DOYLE AND REYNOLDS — Naval Research Laboratory, Monterey, California; MCTAGGART-COWAN — Meteorological Service of Canada, Dorval, Canada; GRAY, HARVEY AND METHVEN — Department of Meteorology, University of Reading, Reading, United Kingdom, UK; RIVIÈRE — École Normale Supérieure/CNRS/UPMC, Paris, France; CREWELL, JACOB AND MECH — Universität Köln, Köln, Germany; CAZENAVE, DELANOË AND PELON — Laboratoire ATmosphère, Milieux, et Observations Spatiales (LATMOS), Guyancourt, France; COTTON — Met Office, Exeter, United Kingdom; EHRLICH, WENDISCH AND WOLF — Universität Leipzig, Leipzig, Germany; HIRSCH — Max Planck Institute for Meteorology, Hamburg, Germany; AMENT AND KONOW — Universität Hamburg, Hamburg, Germany and Max Planck Institute for Meteorology, Hamburg, Germany; MAGNUSSON — European Centre for Medium-Range Weather Forecasts, Reading, United Kingdom; MOORE — Norwegian Meteorological Institute / University of Oslo, Oslo, Norway; QUINTING — ETH Zürich, Switzerland and Monash University, Clayton, Australia; RAUTENHAUS — Technische Universität München, Garching, Germany; SODEMANN AND SPENGLER — Geophysical Institute, University of Bergen and Bjerknes Centre for Climate Research, Bergen, Norway; VAUGHAN — National Centre for Atmospheric Science, University of Manchester, Manchester, United Kingdom

Corresponding author:

Dr. Andreas Schäfler, Institut für Physik der Atmosphäre, Deutsches Zentrum für Luft- und Raumfahrt (DLR), Oberpfaffenhofen, 82234 Weßling, Germany, email: andreas.schäfler@dlr.de

Capsule. Multi-aircraft and ground-based observations were made over the North Atlantic in fall 2016 to investigate the importance of diabatic processes for mid-latitude weather.

Abstract. The North Atlantic Waveguide and Downstream Impact Experiment (NAWDEX) deployed four aircraft with a sophisticated set of remote-sensing and in-situ instruments, coordinated with ground-based measurements. A total of 49 research flights were performed, including, for the first time, coordinated flights of the four aircraft; the High Altitude and LOng Range Research Aircraft (HALO), the Deutsches Zentrum für Luft- und Raumfahrt (DLR) Falcon 20, the French Service des Avions Français Instrumentés pour la Recherche en Environnement (SAFIRE) Falcon 20, and the Facility for Airborne Atmospheric Measurements (FAAM) BAe 146. The observation period from 17 September to 22 October 2016 was ideal to investigate the influence of diabatic processes on the jet stream evolution, with frequently occurring extratropical and tropical cyclones in the North Atlantic. NAWDEX focused on upstream triggers of waveguide disturbances, their dynamic interaction with the jet stream, the subsequent downstream development, and the eventual weather impact on Europe. The campaign period featured three such sequences, and included observations of the extra-tropical transition of tropical storm Karl, its intensification through interaction with the jet stream, and a sequence of downstream events that eventually led to high-impact weather in NW Europe. Examples are presented to highlight the wealth of phenomena that were sampled, the comprehensive coverage and the multi-faceted nature of the measurements. This unique data set forms the basis for future case studies and detailed evaluations of weather and climate predictions to improve understanding of diabatic influences on Rossby wave propagation and downstream impact of weather systems hitting Europe.

Progress in understanding the processes controlling mid-latitude weather has contributed to a continuously improvement in the skill of medium-range weather forecasts in recent decades (Thorpe 2004; Richardson et al. 2012). At the same time, the fundamental limits of predictability have been recognized in practice, with the development and widespread use of ensemble prediction systems (EPS) to represent forecast uncertainty (Bauer et al. 2015). However, the short-term prediction of high-impact weather (HIW) events (e.g., strong winds and heavy precipitation), and the medium-range prediction of extratropical cyclones, their tracks and intensity is still a major challenge (e.g., Frame et al. 2015). Recent research on mid-latitude weather has focused on quantifying model errors and predictability, and in particular on investigating the role of diabatic processes such as those related to clouds and radiation, whose interaction with the dynamics of the flow must be understood and represented more accurately in models in order to further improve forecast quality.

Detailed observations are needed to characterize the weather systems and embedded physical processes across a range of spatial and temporal scales that encompasses cloud microphysical variability and Rossby waves. In September and October 2016, the North Atlantic Waveguide and Downstream Impact Experiment (NAWDEX) made new multi-scale observations in the North Atlantic basin from eastern Canada to Western Europe. Weather features expected to be associated with downstream errors in operational forecasts were extensively observed to provide an independent and high-quality data set.

The fall season was chosen for the experiment because at this time diabatic processes are particularly active due to relatively high sea surface temperatures, and the jet stream intensifies as the high latitudes cool. Many of the weather phenomena central to the growth of disturbances on the jet stream and mid-latitude predictability are active in autumn, such as extratropical cyclones with intense fronts and warm conveyor belts (WCB), carrying air from the oceanic boundary layer into ridges at tropopause level. There is also the possibility of North Atlantic tropical cyclones (TC) recurving poleward into mid-latitudes and undergoing extratropical transition (ET) – a process known to be associated with low predictability (Harr et al. 2008). And finally, mesoscale depressions of the tropopause, so-called tropopause polar vortices (TPVs, Cavallo and Hakim 2010; Kew et al. 2010), can disturb the jet stream if they move equatorward from the Arctic.

The concept of the field campaign emerged from the World Meteorological Organization's (WMO) THORPEX (The Observing-System Research and Predictability Experiment) program (Parsons et al. 2017) and the campaign contributes to the World Weather Research Program (WWRP) and its High Impact Weather project (Jones and Golding 2015). NAWDEX aims to provide the observational foundation for further investigating cloud diabatic processes and radiative transfer in North Atlantic weather systems, which will form the basis for future improvements in the prediction of HIW over Europe from short-range weather forecasts to climate projections.

THE ROLE OF DIABATIC PROCESSES. Weather in Europe strongly depends on the life-cycle of Rossby waves that propagate along the slowly-varying part of the North Atlantic jet stream (Martius et al. 2010). The strong meridional potential vorticity (PV) gradient associated with the jet stream serves as waveguide for propagating Rossby waves. Frequently, small disturbances in the jet entrance region over eastern North America grow in baroclinic weather systems and evolve into large-amplitude features in the European sector (Schwierz et al. 2004). Figure 1 portrays an idealized North Atlantic flow situation that could result in high impact weather (HIW) in the form of high winds and heavy precipitation over northern Europe. In addition to Rossby waves amplifying through baroclinic instability, diabatic processes are able to modify upper-tropospheric PV at the level of the mid-latitude jet stream, which impacts the wavelength and amplitude of the downstream Rossby wave development (e.g., Massacand et al. 2001; Knippertz and Martin 2005; Grams et al. 2011).

The majority of precipitation and cloud diabatic processes in extratropical cyclones occur within a coherent airstream known as the WCB. This ascending airflow carries warm, moist air from the low-level warm sector of a cyclone to the ridge at tropopause level within 1-2 days (Browning et al. 1973; Carlson 1980; Wernli and Davies, 1997). The boundary layer humidity in the inflow of WCBs (Region 1 in Fig. 1) can impact the outflow height of WCBs (Schäfler and Harnisch 2015). During the ascent of WCBs (Region 2 in Fig. 1), latent heating due to cloud microphysical processes, embedded convection and turbulent fluxes influence the level of the outflow layer, the direction taken by outflow air masses, and the shape of the upper-level ridge (Martínez-Alvarado et al. 2014; Joos and Forbes 2016). The latent heating in WCBs is strong both in the early phase of the ascent when condensation dominates and later when mixed-phase clouds are formed and vapor deposition on ice crystals and snow becomes important (Joos and Wernli 2012). The effect of the heating on the PV structure is to produce a positive PV anomaly in the lower troposphere (Wernli and Davies 1997), which influences the structure and evolution of mid-latitude cyclones (e.g., Kuo et al. 1991; Davis et al. 1993; Binder et al. 2016). Above the level of maximum latent heating, PV is reduced by cloud diabatic processes leading to negative PV anomalies in the upper-tropospheric WCB outflow region (Wernli 1997; Pomroy and Thorpe 2000; Madonna et al. 2014; Methven 2015). The divergent outflow winds (Region 3 in Fig. 1) tend to amplify the upper-level downstream ridge and to intensify the jet stream by strengthening the PV gradient (Archambault et al. 2013). If the outflow layer is higher, the negative PV anomaly is stronger and more air mass enters the anticyclonic branch of the WCB flowing into the downstream ridge (Grams and Archambault 2016). In addition, a sharp peak in longwave radiative cooling near the tropopause, associated with a step change in water vapor, creates a reinforcement of the positive PV anomaly in upper-level troughs (Chagnon et al. 2013).

Diabatic processes also play a key role in weather systems that act as triggers to disturb the mid-latitude waveguide. Recurving TCs undergoing ET (Jones et al. 2003) can enhance the anticyclonic flow at upper levels, excite Rossby waves and cause downstream forecast errors, as well as HIW events (e.g., Agusti-Panareda et al. 2004; Harr et al. 2008; Riemer and Jones 2010), and radiatively-maintained TPVs, which are positive PV anomalies above the tropopause, can disturb the Rossby waveguide from polar latitudes.

Rossby wave breaking leads to PV filamentation forming smaller-scale PV anomalies such as PV streamers and cut-off vortices. They form frequently over the eastern North Atlantic and Europe (e.g., Wernli and Sprenger 2007), and several studies have reported their relevance for triggering HIW, in particular heavy precipitation (e.g., Martius et al. 2006; Chaboureau and Claud 2006; Grams and Blumer 2015). Synoptic wave breaking events are also important for the large-scale flow itself as they reinforce weather regimes such as blocking ridges (Michel and Rivière 2011; Spensberger and Spengler 2014). However, blocks are also strongly influenced by diabatic processes in air masses ascending from the lower troposphere (Pfahl et al. 2015).

Disturbances of the waveguide and errors can amplify and propagate downstream, and may cause significant forecast errors over Europe (Madonna et al. 2015; Martínez-Alvarado et al. 2016) (Region 4 in Fig. 1). In numerical weather predication (NWP) models, diabatic processes such as convection, cloud microphysics and radiation are represented by parameterizations of varying degrees of fidelity and may contain both systematic and random errors that influence forecast skill. A distinct Rossby wave pattern associated with poleward transport of warm and moist air over the eastern US and strong diabatic activity has been identified as a common precursor 6 days before the worst forecast busts over Europe (Rodwell et al. 2013). Upscale error growth experiments in numerical models show that perturbations grow most rapidly where condensation occurs before expanding in scale to affect the synoptic-scale weather pattern (Zhang et al. 2007; Selz and Craig 2015). Doyle et al. (2014) found forecasts of an extratropical cyclone with severe impact in Western Europe to be very sensitive to the initial low-level moisture, which influenced the moisture supply in a

WCB. At upper levels, global NWP models fail to maintain the strong tropopause sharpness, which decreases with forecast lead time (Gray et al. 2014). This can have major implications for the representation of the downstream propagation and amplification of Rossby waves in NWP (Harvey et al. 2015) and the associated prediction of HIW.

Previous studies using measurements to study the influence of diabatic processes on the Rossby wave guide have been primarily based on routinely collected observations by operational meteorological services. These observations rely largely on satellite data, mainly in cloud-free areas, and sparse in-situ measurements that are combined in the data assimilation system using model information as a background estimate. This approach is not fully adequate to study diabatic processes since these processes tend to be strongest in cloudy regions, which are characterized by a high-degree of small-scale variability. In the last decade, airborne research into mid-latitude weather systems was coordinated by the WWRP program THORPEX. A series of field campaigns, including the Atlantic THORPEX Regional Campaign (ATReC, Rabier et al. 2008), Winter Storm Reconnaissance (WSR, e.g., Szunyogh et al. 2000), THORPEX Pacific Asian Regional Campaign (T-PARC, Weissmann et al. 2011), and Convective and Orographically-induced Precipitation Study (COPS)/European THORPEX Regional Campaign (ETReC 2007, Wulfmeyer et al. 2011) focused on the evaluation of the impact of enhanced observations, especially those in so-called sensitive regions that were identified on the basis of theoretical models of dynamical error growth. Later, in THORPEX the focus shifted towards the investigation of diabatic processes and their relevance for predictability. Two single-aircraft pre-campaigns were crucial in defining the science goals of NAWDEX. DIAbatic influence on Mesoscale structures in ExTratropical storms (DIAMET, Vaughan et al. 2015) made in-cloud measurements to examine the role of diabatic processes in mesoscale weather systems over the UK. The THORPEX-NAWDEX-Falcon project (Schäfler et al. 2014) carried out in-situ observations of clouds, humidity and wind in ascending WCBs, including the Lagrangian re-sampling of air masses.

EXPERIMENTAL DESIGN AND OBSERVATIONS. The central hypothesis of NAWDEX is that diabatic processes have a major influence on the jet stream structure, the downstream development of Rossby waves, and eventually HIW. To evaluate this hypothesis the NAWDEX international consortium formulated a number of specific science goals which are summarized in Table 1. A combination of aircraft with a sophisticated set of instruments was assembled, in coordination with ground-based observations at many sites covering the North Atlantic basin and large parts of Europe. This constellation enabled detailed observations of the phenomena depicted in Fig. 1, including triggering disturbances on the North Atlantic wave-guide, their interaction with the jet stream, the downstream development, and their potential impact on weather over Europe from the western Mediterranean to Scandinavia. NAWDEX observations took place in the North Atlantic basin between 17 September and 22 October 2016.

Airborne platforms and payload. NAWDEX employed four research aircraft, the German High Altitude and LOng Range Research Aircraft (HALO), the Deutsches Zentrum für Luft- und Raumfahrt (DLR) Dassault Falcon 20, the French Service des Avions Français Instrumentés pour la Recherche en Environnement (SAFIRE) Falcon 20, and the British Facility for Airborne Atmospheric Measurements (FAAM) BAe 146. The payload was chosen to observe profiles of wind, temperature, moisture and cloud properties, and in case of FAAM, in-situ cloud microphysics. HALO and the two Falcon aircraft operated from Keflavik, Iceland, in an area covering the North Atlantic north of 35° N and Northern and Central Europe; FAAM operated from northern UK.

The strategy was to deploy HALO with its extended range to observe diabatic processes in upstream weather systems that impact the mid-latitude wave-guide. HALO is a modified Gulfstream G-550 ultra-long-range business jet with a maximum flight range of about 10000 km and a long endurance of up to 10 hours (Krautstrunk and Giez 2012; Wendisch et al.

2016), which allows accessing remote regions over the central North Atlantic that are not accessible by other European research aircraft. The high ceiling of almost 15 km in combination with a sophisticated remote-sensing payload (see sidebar and Table 2) allow HALO to fly above the main commercial aircraft routes and to probe features of interest from above. The two Falcon aircraft, with a maximum range of 3000 km, a maximum endurance of about 4 hours and a ceiling up to 12 km, aimed to observe the approaching cyclones and evolving jet streams close to Iceland. The DLR Falcon was equipped with two wind lidar systems and the SAFIRE Falcon with a remote-sensing payload for clouds and winds (sidebar and Table 2). The FAAM BAe 146, with a maximum endurance of 5 hours and a ceiling of 10 km, was equipped with a range of in-situ instrumentation for meteorological, cloud and chemical measurements together with a downward-pointing aerosol lidar and passive spectral radiometers. Its flights from East Midlands, UK, aimed at observing microphysics and turbulence in WCBs and the structure of the jet stream.

HALO, SAFIRE and the FAAM aircraft were equipped with dropsonde dispensers to measure air temperature, wind and humidity profiles. Global NWP centers could access the dropsonde data from HALO and SAFIRE via the Global Telecommunication System (GTS) in near real-time. The potential for coordinated application of the various instruments on board multiple aircraft was realized through specific instrument-driven science goals (Table 1).

In parallel to NAWDEX, the NOAA (National Oceanic and Atmospheric Administration) SHOUT (Sensing Hazards with Operational Unmanned Technology) campaign took place in the tropical and subtropical western North Atlantic. SHOUT utilized the unmanned NASA Global Hawk aircraft with a suite of remote-sensing platforms and dropsondes to study the impact of the observations on TC forecasts. During the campaign, a tropical storm (TS) moved into the mid-latitudes and underwent ET, providing an unprecedented scientific opportunity to observe the interaction of such a system with the jet stream using a combination of upstream flights with the SHOUT Global Hawk and downstream flights with NAWDEX aircraft.

[Place Sidebar 1 here: Active remote-sensing observations for future satellite missions Aeolus and EarthCARE]

Flight strategy and flight planning. Performing research flights over the North Atlantic is a complicated task because of the dense trans-Atlantic air traffic. Commercial airliners are tightly staggered along predefined flight routes, the North Atlantic Tracks (NATs), between altitudes of 9 and 12 km. Operating research aircraft beneath the NATs offers high flexibility for the flight planning; however, the base height of the NATs is often too low to allow observations of the tropopause and jet-related maximum wind speeds. Furthermore the location of the NATs changes from day to day, depending on the forecast wind situation. Height changes and the release of dropsondes from high altitudes are not possible in the NAT area. North of about 61°N in Icelandic and Greenland airspace, more complicated flight patterns are possible due to reduced traffic and radar control, which is essential to obtain flight plan approval by Air Traffic Control (ATC).

A research flight is planned to meet specific science objectives, but constrained by aircraft capabilities and the need for ATC approval. The patterns designed by the scientists must be converted into a precise flight plan and submitted to ATC by the aircraft operation specialists. The requirement of ATC authorities to have detailed flight plans 2-3 days in advance created challenging circumstances in weather situations with reduced predictability, i.e., in situations with large changes between subsequent forecasts. Therefore, NAWDEX combined modern forecasting tools including ensemble and adjoint-based diagnostics and new visualization techniques to incorporate forecast uncertainty in the planning process (see sidebar on forecast products). Preparing several scenarios for the upcoming flights helped adapting flight plans quickly during the planning phase. The pilots reviewed the feasibility of the proposed flights, and, together with the flight planning team, considered the possibility of adverse meteorological conditions near the airport and during the flight such as high wind speeds, turbulence, and cloud and icing conditions.

[Sidebar 2: Forecast products to investigate forecast uncertainty]

Airborne observations. Figure 2 shows the tracks of the 49 research flights of the four aircraft, together amounting to 205 flight hours. HALO covered large parts of the central and eastern North Atlantic and reached flight distances up to 7150 km (~9 h). The flights were performed at altitudes between 11.5 and 14.2 km for remote-sensing observations and at ~8 km to release dropsondes beneath the NATs. The Falcons remained in radar-controlled air spaces near Greenland, Iceland and the UK. The FAAM BAe 146 flights were north and west of the UK. A total of 289 dropsondes were released (Fig. 3a).

The research flights are assigned to 13 Intense Observation Periods (IOPs), which were consecutively numbered and had a duration of 1-6 days. Each IOP was associated with a particular weather system development and addressed one or more NAWDEX science objectives (Table 3). For easier communication, the IOPs were given names, which either correspond to the (tropical) cyclone naming of the Free University of Berlin or the National Hurricane Center, or were invented by the NAWDEX team (Table 3). Some IOPs overlap in time when different weather systems were observed simultaneously by the different aircraft.

To exploit instrument synergies and enable direct instrument comparisons, coordinated flights were performed, i.e., the same air mass was near-simultaneously probed by different aircraft on common flight legs. In total, 16 coordinated flight legs with a total flight time of 14.5 h and a distance of about 10 000 km were achieved. The longest coordinated leg with the SAFIRE Falcon and HALO on 14 Oct 2016 had a distance of 1365 km (1.8 h). On two occasions the coordination involved three aircraft: HALO and the two Falcons flew together for ~30 min (~300 km) on 9 Oct between the UK and Iceland, and on 14 Oct, FAAM, HALO and the SAFIRE Falcon had a common leg between the Faroe Islands and Scotland (55 min, 570 km).

Ground-based facilities and observations. During several IOPs additional ground-based observations were taken to complement the aircraft operations and to enhance the temporal and spatial coverage of routine observations. In total 589 additional radiosondes from 40 different stations in 14 different countries were launched (Fig. 3b and Table 4). 253 of these launches were achieved through the cooperation of national meteorological agencies in the European Meteorological Services Network (EUMETNET), complemented by additional radiosondes from Iceland, UK, France and Norway. Launches from land stations or commercial ships were requested daily depending on the predicted evolution of weather systems. Furthermore, two additional radiosondes were launched daily during the campaign from six stations in eastern Canada, upstream of the main NAWDEX area (336 in total).

Special ground-based observations were conducted in Iceland, the UK and France (Fig. 3b). At Keflavik airport, a radiosonde facility was set up by DLR to increase the frequency of the operational soundings. In cases of orographically-induced gravity waves (GWs), large balloons were launched to reach altitudes up to 42 km. Also in Keflavik, a Doppler cloud radar BASTA (Delanoë et al. 2016) allowed several comparisons with its airborne counterpart on board the SAFIRE Falcon during overflights. In the UK, a mesosphere–stratosphere–troposphere (MST) radar, Raman lidar, and radiosondes were operated at Capel Dewi (Wales), together with another MST radar wind profiler at South Uist (Scotland). Additionally, the MST radar at Andøya, Norway, measured tropospheric winds upon request. Two observational super-sites were active in France during the campaign. The site in Lannion (Brittany) operated a wind profiler, the BASTA Doppler cloud radar and a GPS station. The SIRTA site near Paris (Haeffelin et al. 2005) operated radar and lidars, and launched radiosondes.

METEOROLOGICAL CONDITIONS. The autumn of 2016 was an unusually favorable period for observing mid-latitude weather over the North Atlantic. The synoptic situation was characterized by an increased frequency of several relevant weather systems compared to climatology (Fig. 4). One of the most prominent features was a strong and long-lasting blocking high and surface anticyclone covering large parts of Scandinavia (Fig. 4a). In contrast, extratropical cyclones were observed more frequently than normal south of Iceland and Greenland (Fig. 4b), in the core area of airborne NAWDEX observations. Consistent with the increased frequency of cyclones, the WCB frequency (Fig. 4c) shows an increased activity over large parts of the North Atlantic. Conversely, the successive poleward transport of warm air and the continuous ascent of low-PV air into the upper troposphere strengthened the downstream anticyclone. Most mid-latitude cyclones (Fig. 4d) approached Iceland from the southwest, which was favorable for reaching them with Falcon flights from Keflavik. Only a small fraction of the extratropical cyclones moved into Central and Northern Europe. Six TS occurred during NAWDEX. Ian (12-16 Sep), Julia (13-16 Sep), Karl (14-25 Sep) and Lisa (19-25 Sep) did not exceed TS strength, while Matthew (29 Sep-9 Oct) and Nicole (4-18 Oct) were classified as major hurricanes. Ian, Karl and Nicole underwent ET and moved far into the mid-latitudes. TPVs originating over the Canadian polar region were observed twice when they moved southward over the Davis Strait and interacted with the mid-latitude wave-guide.

Classifying North Atlantic weather regimes during NAWDEX shows Scandinavian blocking to be the dominant regime (Fig. 5a), corresponding to the anomalous anticyclone activity over northern Scandinavia (Fig. 4a). In late September the block dissolved and a short period with a positive North Atlantic Oscillation (NAO) prevailed before the Scandinavian blocking pattern was again established.

A broad measure of forecast quality during NAWDEX is provided by the anomaly correlation coefficient (ACC) of the mid-tropospheric geopotential height pattern over the eastern North Atlantic as predicted by the ECMWF Integrated Forecasting System (IFS) for the entire autumn 2016 (Fig. 5b). Periods of increased 5-day forecast errors and high spread in the ensemble forecasts are evident, and four of these periods were directly relevant to NAWDEX. The high forecast uncertainty from 11 to 14 September took place ahead of the campaign period, but complicated the planning of the transfer flight to Keflavik five days later. The other three periods of reduced forecast skill appeared during NAWDEX and two of them are accompanied by a weather regime transition (Fig. 5a). Forecast uncertainty was high on 26 September during the onset of a positive NAO phase, and on 1 October during the return to the Scandinavian blocking regime.

The progression of weather systems across the North Atlantic can be conveniently described as a storyline characterized by *upstream triggers*, their dynamic *interaction* with the jet stream, *downstream development* of the disturbances, and *weather impact* on Europe. Three such sequences occurred completely within the NAWDEX period, and their timespan is indicated by dark grey shading in Fig. 5. In each case, low predictability was found in 5-day forecasts for the eastern Atlantic region that were initiated within the *trigger* stage (Fig. 5b), while the final *impact* stage was associated with significant changes in the weather over Europe. However, the specific weather systems associated with the four stages differed markedly between the three sequences (Fig. 6), and the observation strategy shown in the conceptual diagram of Fig. 1 had to be adapted for each IOP within each sequence. A number of coherent long-lived features are labelled in the snapshots in Fig. 6 (identified in the caption). Prominent ridges (R1-R9) along the North Atlantic waveguide are identified as northward excursions of the jet stream (and the PV gradient). Since each ridge is characterized by low PV air, the associated flow tends to be anticyclonic.

Sequence A is *triggered* by TS Karl leaving the subtropics and moving northwards into the mid-latitudes (Fig. 6, panel A.1). The subsequent evolution was very sensitive to uncertainties it the location and timing of the interaction of Karl with ridge R2, the tropopause trough upstream, and the associated weak surface cyclone. The *interaction* that in fact took place was a merging of Karl with a low-level cyclone, leading to rapid re-intensification and the formation of a cyclonic hook at tropopause level separating ridge R2 from the new ridge R3 (Fig. 6 A.2). The ridge-building is intensified by diabatically-produced low PV in WCB outflows. Hence in the subsequent *development*, the jet stream is unusually strong on its southern flank forming a jet streak that shoots ahead from Karl reaching Scotland the following day (Fig. 6 A.3). The *impact* on European weather occurs through the formation of a new cyclone Walpurga (W in Fig. 6 A.4), which develops to the west of ridge R3 helping to amplify it. Moisture laden air on the western flank of ridge R3 is drawn around the subtropical high as an atmospheric river (Cordeira et al. 2013) that extends to Norway where it causes heavy, persistent rainfall, similar to the case studied in Sodemann and Stohl, 2013.

Sequence B begins as sequence A ends, in a southwesterly flow situation with a long PV streamer that formed through the merger of the trough west of R3 and the large cut-off feature C (Fig. 6 A.3-A.4). The *trigger* for this sequence appears to follow from the vortex roll-up of the streamer through shear instability, resulting in a new cut-off over Newfoundland (Fig. B.1), which then *interacts* and merges with a large-scale trough advancing rapidly from the northwest. Note that ridge R5 and its upstream trough wrap up cyclonically during the development so that the trough catches up with the cut-off to the south of R5. The tropopause was very low just in the very center of this system, which therefore has been named the "stalactite cyclone" (St in Fig. 6 B.2). In the *development* stage (Fig. 6 B.3), a second cyclone (F) intensified rapidly between ridge R6 and the trough to its west. The poleward moving air in R6 crossed Iceland and reinforced the anticyclonic anomaly formed by ridge R5 of the stalactite cyclone. The *impact* of the sequence comes not as a classical severe weather event, but through the establishment of a strong dipole block over Europe, which persisted for the next two weeks. The block had impact on the Arctic sea ice causing a very late onset of sea ice formation in Svalbard that fall.

Sequence C begins with two upstream *triggers*. A TPV originating in the Canadian Arctic is carried rapidly southeastwards on the poleward flank of the jet stream. It is hypothesized that the TPV locally enhanced the cyclonic circulation about the tip of the large-scale trough (T in Fig. 6 C.1), which eventually wrapped cyclonically over Iceland (Fig. 6 C.2). At the same time the remnants of cut-off C appear instrumental in spinning up a small surface cyclone, which has been named “Sanchez” (S in Fig. 6 C.1). The European dipole block is well established at this time so that the ridge R8 and cyclonic PV anomaly over Iceland are held stationary and a PV filament forms in the deformation region on their western side. The filament is unstable and experiences vortex roll-up, forming three tropopause level cyclonic vortices. The key *interaction* in this sequence occurs as the low-level cyclone Sanchez passes the southernmost cut-off, but then phase-locks with the central cut-off resulting in baroclinic intensification (S in Fig. 6 C.2). As the sequence *develops*, the resulting cut-off cyclone progresses slowly eastwards (Fig. 6 C.3) and is responsible for some of the most dramatic high *impact* weather during NAWDEX, with heavy precipitation and flooding across southern France and northwestern Italy in the southerly flow ahead of it (Fig. 6 C.4). But this is not the only significant *impact* resulting from Sequence C. Returning to stage C.2, ridges R8 and R9 are similar in horizontal extent, but the tropopause is much higher above R9 than R8 with the result that the anticyclonic circulation induced by R9 is mightier and R8 is stretched out meridionally between R6 and R9 (Fig. 6 C.3). As NAWDEX draws to a close, the ridge R9 extends rapidly into the Arctic reinforcing the block and forming a PV anomaly in the shape of the Icelandic character Þ (the first letter of Þor – pronounced Thor - the ancient Norse god of HIW).

HIGHLIGHTS OF NAWDEX. Observations in NAWDEX were organized in IOPs that focused on key weather systems involved in the longer sequences. Several of these are unprecedented in terms of the phenomena that were sampled or the comprehensive coverage and multi-faceted nature of the measurements and are described briefly in Table 5. While the analysis of the data is just beginning, a first impression of the results can be obtained from four highlights that illustrate the unique multi-platform and multi-instrument observations that were obtained.

Extratropical transition of TS Karl. The evolution of TS Karl is the central feature of Sequence A discussed above. It was the first extratropical transition sequence that has been observed with research aircraft at all stages of development, including TS status, ET, re-intensification and downstream impacts on jet stream strength, moisture flow and HIW. By flying over the TS and its northwestern flank twice, the SHOUT Global Hawk observed the development stage that occurred far south of the mid-latitude jet stream on 22/23 September (Fig. 7a), and the ET phase on 24/25 September (Fig. 7b). On 26 September, as part of IOP4, HALO observed the interaction with the waveguide and re-intensification phase of the storm (Fig. 7c) by flying over the cyclone center, WCB ascent, the low-valued PV air in the WCB outflow and the dry intrusion. When Karl moved rapidly towards Scotland, decaying in the strong shear on 27 September, IOP5 with flights of HALO, FAAM and DLR Falcon focused on the intense jet streak at tropopause level and the strong moisture transport to the south of the jet (Fig. 7d). The large number of dropsonde and special radiosonde measurements that were assimilated into operational forecasts in real-time will provide the basis for observational impact and predictability studies. Meanwhile detailed airborne remote-sensing observations will allow examination of the role of diabatic processes and their representation in numerical models. Both the synergies of the instruments and the storm-following observation strategy give unprecedented information about this intense and long-lived cyclone and a chance to analyze error growth in the forecast systems due to in-situ processes vs. downstream propagation.

Cloud physics in a WCB. IOP3 focused on observing the vertical cloud structure and cloud microphysical processes in a WCB that was related to the mid-latitude cyclone Vladiana south of Iceland and west of Scotland on 23 September 2016 (Fig. 7a and Table 5). The WCB transported moist air masses northeastward just west of the UK as can be seen by the low-valued PV air that is brought to the upper troposphere (Fig. 8c).

HALO first stayed beneath the NATs at low altitudes of ~8 km on the way to the southwestern-most point of the flight (white circle) to begin the first of three sections across the WCB. On this leg to Ireland, 12 dropsondes were released before HALO climbed to ~13 km in Irish airspace. Over Northern Ireland, HALO and FAAM joined to perform coordinated remote-sensing and in-situ observations of the WCB. HALO measured the WCB by remote-sensing from above while FAAM performed 4 in-situ legs at different altitudes to measure cloud-microphysical parameters inside the WCB. After the coordinated leg, HALO crossed the WCB a third time and observed the outflow of the WCB between Scotland and Iceland.

Figure 8 focuses on the first and second crossing of the WCB. The WALES lidar measures water vapor profiles throughout the troposphere and lower stratosphere in the absence of clouds. At the western side of the cross-sections, where HALO was located on the stratospheric side of the waveguide, the post-frontal troposphere was cloud-free except for boundary layer clouds reaching up to 2 km. The water vapor shows high variability, which portrays the dynamically-modulated transport of moisture related to cyclone Vladiana. On both crossings of the waveguide, one west-to-east and one east-to west, a tilted dry layer is visible at altitudes between 5 and 9 km (1110-1125 and 1305-1325 UTC), related to a dry intrusion west of the low-level cold front. The wedge-shaped moist layer on top is associated with high moisture values in the WCB outflow. The second crossing at high altitudes depicts a strong vertical moisture gradient on top of the elevated moist layer that marks the tropopause and extends further east into the area where WCB clouds reach high altitudes. A decrease of the tropopause height is detected towards the west on the second leg. The radar shows two vertically (~11.5 km) and horizontally (~400 km) extended and coherent clouds (Fig. 3b) representing the double crossing of the WCB. In between, i.e., on the eastern side of the WCB, cloud tops are lower and the clouds intermittent. The sharp vertical gradient in radar reflectivity at about 3 km altitude marks the melting layer.

On the second transect the FAAM aircraft performed in-situ measurements on flight legs beneath HALO (Figs. 8a,b). HALO met FAAM at the beginning of its second WCB leg where FAAM started its lowest leg at about 3 km altitude, just above the melting layer, with subsequent legs at 4, 6 and 7.5 km. The in-situ observations show that both mixed-phase and ice-only clouds were encountered during the low-level run, but during the high-level runs only ice was observed. The ice water content (IWC) in the WCB shows maximum values of 0.4 g m^{-3} on the lowest two legs. Ice images showed large differences in the form of the particles at different altitudes. On the lowest leg, large aggregates (~6 mm) dominated close to the freezing level, while on the highest level higher concentrations of small irregularly shaped crystals (< 1 mm) prevailed.

HALO also observed the interaction of Vladiana's WCB outflow with the jet stream in coordination with the DLR Falcon (not shown). IOP3 contributes to all research topics (Table 3) and future work on the cloud microphysics observations will investigate, e.g., the correlation of increased IWCs with particularly high radar reflectivities. Data from liquid and ice particle size distributions will be used to improve the retrieval of cloud properties from the HALO remote-sensing instruments. Overall, this is clearly a unique case of comprehensive and complementary airborne observations of a WCB, its embedded microphysical processes and its outflow interaction with the jet stream.

Wind observations in the jet stream and outflow of a WCB. Figure 6 (panel B.2) shows the stalactite cyclone that formed when two near-surface vorticity maxima merged with a very intense, small-scale, upper-level PV anomaly south of Newfoundland. The rapid development of the cyclone occurred in the mid-Atlantic between 30 Sep and 02 Oct. On 02 Oct (IOP6), a coordinated flight of the DLR and SAFIRE Falcons observed WCB ascent and outflow when the stalactite cyclone was at its most intense (Fig. 9c). The aircraft flew together to intersect the waveguide on the northwestern edge of ridge R5 wrapping cyclonically around the stalactite cyclone. On a common leg between Iceland and Greenland both aircraft crossed the jet stream (Fig. 9d) and made complementary wind observations (Figs. 9a,b). The DWL lidar on the DLR Falcon observed two wind maxima up to 50 m s^{-1} in cloud-free regions and in optically thin cirrus in the WCB outflow. Complementarily, the SAFIRE radar observed in-cloud winds in the region of WCB ascent in the mid and lower troposphere. Only in dry and aerosol-poor air masses over Greenland, i.e., on the stratospheric side of the waveguide, the combination of both instruments provides poor data coverage. The SAFIRE Falcon released 9 dropsondes when crossing the jet stream, yielding further profiles of winds, temperature and moisture.

Future research on this case will be mainly dedicated to predictability issues associated with the blocking formation downstream of the cyclone. The block formed at the time when a loss of predictability in the ECMWF forecasts occurred (Fig. 5b). Winds measured by the two aircraft will help characterizing the role of the WCB outflow in the ridge building. The observed high winds and strong vertical gradients were repeatedly observed on flights across the jet stream with observed maxima up to 80 m s^{-1} and often related to strong vertical wind speed gradients up to 30 m s^{-1} km^{-1}. A unique aspect of this example is the benefit of coordinated flights with complementary instruments to address one the key objectives of NAWDEX – the strong wind shear and PV gradients near a WCB outflow.

HIW related to cut-off cyclone Sanchez. Cut-off Sanchez was initiated in the central North Atlantic and reached Southern Europe between 12 and 14 Oct 2016 (Fig. 6, Seq. C). On its leading edge moisture was advected northward (Fig. 10a) on 13 October when it triggered heavy precipitation and strong winds over France and Italy. The accumulated precipitation in the Herault region reached ~250 mm and wind gusts exceeding 100 km h^{-1} were observed along the French Mediterranean coast (Figs. 10c,d). As in usual Cevenol episodes, strong southerlies brought warm and moist air from the Mediterranean Sea toward the Massif Central. Upper-level cut-offs like Sanchez are known to be favorable synoptic conditions for triggering convective mesoscale events (Nuissier et al. 2008), which were intensively studied during the recent international field campaign HyMex (Ducrocq et al. 2016). The transport of moist air masses extended further north and part of the air masses that participated in the HIW event reached Paris, i.e., the SIRTA site, afterwards and caused precipitation in the afternoon of 13 Oct (Fig. 10b). This episode illustrates one of the key NAWDEX hypotheses that some HIW events over Europe are associated with complex waveguide dynamics (in this case the formation of a PV cut-off) over the upstream North Atlantic. The combination of the ground-based supersite data with NAWDEX observations both from aircraft in IOP9 and from the many additional radiosondes taken during Sanchez, will enable detailed studies of the forecast sensitivity of HIW to upstream initial condition errors.

SUMMARY. NAWDEX was the first field experiment with synergistic airborne and ground-based observations from the entrance to the exit of a storm track, in order to investigate the role of diabatic processes in altering jet stream disturbances, their development, and effects on HIW downstream. Elements of the field experiment design built on earlier campaigns that were conducted under the umbrella of THORPEX (Parsons et al. 2017).

The NAWDEX aircraft data set includes high resolution wind, water vapor, and cloud information from different weather systems, taking full advantage of recent developments in remote-sensing instrumentation. Often, the same weather system was sampled at different stages of its development, and successive weather systems have been observed following the NAWDEX storyline (Figs. 1, 6). Additional ground-based observations at supersites and an enhanced density of operational radiosonde releases yielded very high coverage with high-resolution vertical profiles from the ground to the lower stratosphere. The region with enhanced atmospheric profiling extended from eastern Canada to most parts of Europe. The coverage and detail of the resulting data will enable future studies to constrain estimates of diabatic heating in situations when the atmospheric flow is especially sensitive to perturbations. Table 5 lists a number of particular highlights and "firsts" that have drawn the attention of the NAWDEX scientists, and it is an interesting exercise to compare this list with the original campaign objectives in Table 1.

These observations were only possible because of the very favorable meteorological situation during the campaign, with many cyclones and WCBs in the vicinity of Iceland. Importantly, the NAWDEX period contained episodes of reduced predictability, which indicates that the atmosphere was sensitive to processes on different scales, so that uncertainties originating in the estimated atmospheric state and model formulation grew rapidly. NAWDEX therefore provides an excellent opportunity to study predictability issues of mid-latitude weather and the representation of uncertainty in EPS. Since there were also episodes of HIW in Europe connected to disturbances propagating along the wave-guide, NAWDEX allows exploration of the predictability of HIW.

The NAWDEX period is the best observed concerning the North Atlantic jet stream and its legacy will form the basis of case studies and evaluation of weather and climate prediction models for many years. The widespread coverage of high-resolution multi-variate cross-sections across the jet stream and weather systems developing from one side of the North Atlantic to the other enable examination of the whole chain of processes from the triggering of disturbances on the waveguide (e.g., by TS and TPVs), diabatic influences on Rossby wave propagation and the downstream impact on weather systems hitting Europe.

ACKNOWLEDGMENTS. Many international institutions contributed to the implementation of NAWDEX and the results presented in this overview article. NAWDEX was only possibly due to the close cooperation of many colleagues including the planning team, the instrument groups and the flight operations (Appendix A). The HALO and DLR Falcon campaign received funding from DLR (project "Klimarelevanz von atmosphärischen Spurengasen, Aerosolen und Wolken" KliSAW), ETH Zurich, NRL Monterrey, the German Science Foundation (DFG; within SPP1294 HALO and SFB/TRR165 Waves to Weather), the EUropean Facility for Airborne Research (EUFAR, project NAWDEX Influence) and the European Space Agency (ESA, providing funds related to the preparation of Aeolus (WindVal II, contract No. 4000114053/15/NL/FF/gp) and EarthCARE (EPATAN, contract No. 4000119015/16/NL/CT/gp)). Special thanks are due to the Max Planck Institute Hamburg for sharing the HALO payload during the NARVAL-II and NAWDEX campaigns in summer and autumn 2016 and for their general support of NAWDEX. We are grateful to the DLR flight experiments team; in particular the colleagues of flight operations for the careful preparation and the outstanding support in Keflavik. The authors are grateful to the HALO and Falcon pilots and the technical and sensor team from DLR flight operations for excellent support prior and during NAWDEX. The SAFIRE Falcon contribution to NAWDEX received direct funding from IPSL, Météo-France, INSU-LEFE, EUFAR-NEAREX and ESA (EPATAN, contract No. 4000119015/16/NL/CT/gp). The UK funding for the FAAM aircraft flights, dropsondes and additional radiosondes was provided by the Met Office. Observations from the supersite at Capel Dewi were funded by the National Centre for Atmospheric Science. We thank the European Meteorological Service Network (EUMETNET) for funding additional radiosondes and for providing access to the data. Environment and Climate Change Canada provided funding for enhanced radiosonde frequency during the campaign. The Icelandic Meteorological Office and DLR are thanked for providing additional radiosondes from Iceland. We thank ECMWF for providing access to data in the framework of the

Support Tool for HALO Missions (SPDEHALO) special project. We gratefully acknowledge many discussions with US colleagues, in particular Chris Davis, Pat Harr and Heather Archambault, during the scientific preparation of NAWDEX. We thank Michael Sprenger (ETH Zurich) for preparing the data for Fig. 4. MB and CMG acknowledge funding from the Swiss National Science Foundation (Projects 200020_165941 and PZ00P2_148177, respectively. JDD and CAR acknowledge the support of the U.S. Navy Chief of Naval Research through the NRL Base Program PE 0601153N, and the ONR PE 0602435N.

APPENDIX A: The NAWDEX Team

Table A1

REFERENCES

Agusti-Panareda, A., C. D. Thorncroft, G. C. Craig, and S. L. Gray, 2004: The extratropical transition of hurricane Irene (1999): A potential-vorticity perspective. *Quart. J. Roy. Meteor. Soc.*, **130**, 1047-1074.

Archambault, H. M., L. F. Bosart, D. Keyser, and J. M. Cordeira, 2013: A climatological analysis of the extratropical flow response to recurving western North Pacific tropical cyclones. *Mon. Wea. Rev.*, **141,** 2325–2346.

Bauer, P., A. Thorpe, and G. Brunet, 2015: The quiet revolution of numerical weather prediction. *Nature*, **525,** 47–55.

Binder, H., M. Boettcher, H. Joos, and H. Wernli, 2016: The role of warm conveyor belts for the intensification of extratropical cyclones in Northern Hemisphere winter. *J. Atmos. Sci.*, **73**, 3997–4020, doi: 10.1175/JAS-D-15-0302.1.

Brogniez, G., C. Pietras, M. Legrand, P. Dubuisson, and M. Haeffelin, 2003: A high-accuracy multiwavelength radiometer for in situ measurements in the thermal infrared. Part II: Behavior in field experiments. *J. Atmos. Oceanic Technol.*, **20**, 1023–1033.

Browning, K. A., M. E. Hardman, T. W. Harrold, C. W. Pardoe, 1973: Structure of rainbands within a mid-latitude depression. *Quart. J. Roy. Meteor. Soc.* **99**, 215-231.

Bruneau, D., J. Pelon, F. Blouzon, J. Spatazza, P. Genau, G. Buchholtz, N. Amarouche, A. Abchiche, and O. Aouji, 2015: 355nm high spectral resolution airborne lidar LNG: system description and first results. *Appl. Opt.*, **54**, 8776-8785.

Carlson, T. N., 1980: Airflow through midlatitude cyclones and the comma cloud pattern. *Mon. Wea. Rev.*, **108**: 1498–1509.

Cavallo, S. M., and G. J. Hakim, 2010: Composite structure of tropopause polar cyclones. *Mon. Wea. Rev.*, **138,** 3840–3857.

Chaboureau, J.-P., and C. Claud, 2006: Satellite-based climatology of Mediterranean cloud systems and their association with large-scale circulation. *J. Geophys. Res.*, **111**, D01102, doi: 10.1029/2005JD006460.

Chagnon, J., S. Gray, and J. Methven, 2013: Diabatic processes modifying potential vorticity in a North Atlantic cyclone. *Quart. J. Roy. Meteor. Soc.*, **139**, 1270-1282.

Cordeira, J. M., F. M. Ralph, and B. J. Moore, 2013: The development and evolution of two atmospheric rivers in proximity to western North Pacific tropical cyclones in October 2010. *Mon. Wea. Rev.*, **141,** 4234–4255.

Davis, C. A., M. T. Stoelinga, and Y.-H. Kuo, 1993: The integrated effect of condensation in numerical simulations of extratropical cyclogenesis. *Mon. Wea. Rev.*, **121**, 2309–2330.

Delanoë, J., A. Protat, O. Jourdan, J. Pelon, M. Papazzoni, R. Dupuy, J.-F. Gayet, and C. Jouan, 2013: Comparison of airborne in-situ, airborne radar-lidar, and spaceborne radar-lidar retrievals of polar ice cloud properties sampled during the POLARCAT campaign. *J. Atmos. Oceanic Technol.*, **30**, 57-73.

Delanoë, J., A. Protat, J.-P. Vinson, W. Brett, C. Caudoux, F. Bertrand, J. Parent du Chatelet, R. Hallali, L. Barthes, M. Haeffelin, and J.-C. Dupont, 2016: BASTA: A 95-GHz FMCW Doppler Radar for Cloud and Fog Studies. *J. Atmos. Oceanic Technol.*, **33**, 1023–1038, doi: 10.1175/JTECH-D-15-0104.1.

Doyle, J. D., C. Amerault, C. A. Reynolds, and P. Alex Reinecke, 2014: Initial condition sensitivity and predictability of a severe extratropical cyclone using a moist adjoint. *Mon. Wea. Rev.*, **142**, 320-342.

Ducrocq, V., S. Davolio, R. Ferretti, C. Flamant, V. H. Santaner, N. Kalthoff, E. Richard, and H. Wernli, 2016: Introduction to the HyMeX Special Issue on ‘Advances in understanding and forecasting of heavy precipitation in the Mediterranean through the HyMeX SOP1 field campaign’. *Quart. J. Roy. Meteor. Soc.*, **142**, 1-6.

Ehrlich, A., E. Bierwirth, M. Wendisch, J.-F. Gayet, G. Mioche, A. Lampert, and J. Heintzenberg, 2008: Cloud phase identification of Arctic boundary-layer clouds from airborne spectral reflection measurements: test of three approaches. *Atmos. Chem. Phys*., **8**, 7493–7505

ESA European Space Agency, 2008: ADM-Aeolus Science Report, ESA SP-1311, ISBN 978-92-9221-404-3, 121 pp.

Ewald, F., T. Kölling, A. Baumgartner, T. Zinner, and B. Mayer, 2015: Design and characterization of specMACS, a multipurpose hyperspectral cloud and sky imager. *Atmos. Meas. Tech.*, **9**, 2015-2042, doi: 10.5194/amt-9-2015-2016 ISSN 1867-1381

Frame, T. H. A., J. Methven, N. M. Roberts, and H. A. Titley, 2015: Predictability of frontal waves and cyclones. *Wea. Forecasting*, **30**, 1291-1302, doi: 10.1175/WAF-D-15-0039.1.

Grams, C. M., H. Wernli, M. Boettcher, J. Campa, U. Corsmeier, S. C. Jones, J. H. Keller, C. J. Lenz, and L. Wiegand, 2011: The key role of diabatic processes in modifying the upper tropospheric wave guide: a North Atlantic case-study. *Quart. J. Roy. Meteor. Soc.*, **137**, 2174-2193.

Grams, C. M., and S. R. Blumer, 2015: European high-impact weather caused by the downstream response to the extratropical transition of North Atlantic Hurricane Katia (2011). *Geophys. Res. Lett.*, **42**, 2015GL066253, doi:10.1002/2015GL066253.

Grams, C. M., and H. M. Archambault, 2016: The key role of diabatic outflow in amplifying the midlatitude flow: a representative case study of weather systems surrounding western North Pacific extratropical transition. *Mon. Wea. Rev.*, **144**, 3847–3869, doi:10.1175/MWR-D-15-0419.1.

Gray, S. L., C. Dunning, J. Methven, G. Masato, and J. Chagnon, 2014: Systematic model forecast error in Rossby wave structure. *Geophys. Res. Lett.*, **41**, 2979–2987.

Haeffelin, M. , L. Barthès, O. Bock, C. Boitel, S. Bony, D. Bouniol, H. Chepfer, M. Chiriaco, J. Cuesta, J. Delanoë, P. Drobinski, J.-L. Dufresne, C. Flamant, M. Grall, A. Hodzic, F. Hourdin, F. Lapouge, Y. Lemaître, A. Mathieu, Y. Morille, C. Naud, V. Noël, W. O'Hirok, J. Pelon, C. Pietras, A. Protat, B. Romand, G. Scialom, and R. Vautard, 2005: SIRTA, a ground-based atmospheric observatory for cloud and aerosol research. *Annales Geophysicae*, **23,** 1-23.

Harr, P. A., D. Anwender, and S. C. Jones, 2008: Predictability associated with the downstream impacts of the extratropical transition of tropical cyclones: Methodology and a case study of Typhoon Nabi (2005). *Mon. Wea. Rev.*, **128**, 2613–2633.

Harvey, B., J. Methven, and M. Ambaum, 2016: Rossby wave propagation on potential vorticity fronts with finite width. *J. Fluid Mech.*, **794,** 775-797, doi: 10.1017/jfm.2016.180

Illingworth, A.J., H.W. Barker, A. Beljaars, M. Ceccaldi, H. Chepfer, N. Clerbaux, J. Cole, J. Delanoë, C. Domenech, D.P. Donovan, S. Fukuda, M. Hirakata, R.J. Hogan, A. Huenerbein, P. Kollias, T. Kubota, T. Nakajima, T.Y. Nakajima, T. Nishizawa, Y. Ohno, H. Okamoto, R. Oki, K. Sato, M. Satoh, M.W. Shephard, A. Velázquez-Blázquez, U. Wandinger, T. Wehr, and G. van Zadelhoff, 2015: The EarthCARE Satellite: The Next Step Forward in Global Measurements of Clouds, Aerosols, Precipitation, and Radiation. *Bull. Amer. Meteor. Soc.*, **96**, 1311–1332, https://doi.org/10.1175/BAMS-D-12-00227.1

Joos, H., and W. Wernli, 2012: Influence of microphysical processes on the potential vorticity development in a warm conveyor belt: a case-study with the limited-area model COSMO. *Quart. J. Roy. Meteor. Soc*., **138**, 407–418.

Joos, H., and R. Forbes, 2016: Impact of different IFS microphysics on a warm conveyor belt and the downstream flow evolution. *Quart. J. Roy. Meteor. Soc.*, **142,** 2727–2739.

Jones, S. C., P. A. Harr, J. Abraham, L. F. Bosart, P. J. Bowyer, J. L. Evans, D. E. Hanley, B. N. Hanstrum, R. E. Hart, F. Lalaurette, M. R. Sinclair, R. K. Smith, and C. Thorncroft, 2003: The Extratropical Transition of Tropical Cyclones: Forecast Challenges, Current Understanding, and Future Directions. *Wea. Forecasting*, **18**, 1052–1092.

Jones, S. C., and B. Golding, 2015: High Impact Weather Implementation Plan. Available: https://www.wmo.int/pages/prog/arep/wwrp/new/high_impact_weather_project.html

Kew, S. F., M. Sprenger, and H. C. Davies, 2010: Potential vorticity anomalies of the lowermost stratosphere: A 10-yr winter climatology. *Mon. Wea. Rev.*, **138,** 1234–1249.

Knippertz, P., and J. E. Martin, 2005: Tropical plumes and extreme precipitation in subtropical and tropical West Africa. *Quart. J. Roy. Meteor. Soc.*, **131,** 2337–2365.

Krautstrunk, M. and A. Giez, 2012: The transition from FALCON to HALO era airborne atmospheric research. In: *Atmospheric Physics: Background – Methods – Trends Research Topics in Aerospace,* U. Schumann, Ed., Springer-Verlag Berlin, 604-629. Heidelberg, 609–624, ISBN978-3-642-30182-7.

Kuo, Y. H., M. A. Shapiro, and E. G. Donall, 1991: The interaction between baroclinic and diabatic processes in a numerical simulation of a rapidly intensifying extratropical marine cyclone. *Mon. Wea. Rev.*, **119,** 368–384.

Madonna, E., H. Wernli, H. Joos, and O. Martius, 2014: Warm conveyor belts in the ERA-Interim dataset (1979–2010). Part I: Climatology and potential vorticity evolution. *J. Climate*, **27**, 3–26.

Madonna, E., M. Boettcher, C. M. Grams, H. Joos, O. Martius, and H. Wernli, 2015: Verification of North Atlantic warm conveyor belt outflows in ECMWF forecasts. *Quart. J. Roy. Meteor. Soc.*, **141**, 1333–1344, doi:10.1002/qj.244

Marksteiner, U., O. Reitebuch, S. Rahm, I. Nikolaus, C. Lemmerz, and B. Witschas, 2011: Airborne direct-detection and coherent wind lidar measurements along the east coast of Greenland in 2009 supporting ESA´s Aeolus mission. *Proc. of SPIE Remote Sensing*, **8182**, Prague, 19-23 September, 81810J-1 – 81820J-8.

Martínez-Alvarado, O., H. Joos, J. Chagnon, M. Boettcher, S. L. Gray, R. S. Plant, J. Methven, and H. Wernli, 2014: The dichotomous structure of the warm conveyor belt. *Quart. J. Roy. Meteor. Soc.*, **140**, 1809-1824.

Martínez-Alvarado, O., E. Madonna, S. L. Gray, and H. Joos, 2016: A route to systematic error in forecasts of Rossby waves. *Quart. J. Roy. Meteor. Soc.*, **142**, 196–210, doi:10.1002/qj.2645.

Martius, O., E. Zenklusen, C. Schwierz, and H. C. Davies, 2006: Episodes of Alpine heavy precipitation with an overlying elongated stratospheric intrusion: A climatology. *Int. J. Climatol.,* **26,** 1149–1164.

Martius, O., C. Schwierz, and H. C. Davies, 2010: Tropopause-level waveguides. *J. Atmos. Sci.*, **67**, 866–879.

Massacand, A. C., H. Wernli, and H. C. Davies, 2001: Influence of upstream diabatic heating upon an alpine event of heavy precipitation. *Mon. Wea. Rev.*, **129,** 2822–2828.

Mech, M., E. Orlandi, S. Crewell, F. Ament, L. Hirsch, M. Hagen, G. Peters, and B. Stevens, 2014: HAMP – the microwave package on the High Altitude and LOng range research aircraft (HALO). *Atmos. Meas. Tech.*, **7**, 4539–4553.

Methven, J., 2015: Potential vorticity in warm conveyor belt outflow. *Quart. J. Roy. Meteor. Soc.*, **141**, 1065–1071, doi:10.1002/qj.2393.

Michel, C., and G. Rivière, 2011: A link between Rossby wave breakings and weather regime transitions. *J. Atmos. Sci*., **68**, 1730-1748.

Michelangeli, P., R. Vautard, and B. Legras, 1995: Weather Regimes: Recurrence and Quasi Stationarity. *J. Atmos. Sci.,* **52**, 1237–1256, https://doi.org/10.1175/1520-0469(1995)052<1237:WRRAQS>2.0.CO;2

Nuissier, O., V. Ducrocq, D. Ricard, C. Lebeaupin, and S. Anquetin, 2008: A numerical study of three catastrophic precipitating events over southern France. I: Numerical framework and synoptic ingredients. *Quart. J. Roy. Meteor. Soc.*, **134**, 111-130.

Parsons, D. B., and Co-authors, 2017: THORPEX research and the science of prediction. *Bull. Amer. Meteor. Soc.*, **98**, 807–830.

Pfahl, S., C. Schwierz, M. Croc-Maspoli, C.M. Grams, and H. Wernli, 2015: Importance of latent heat release in ascending air streams for atmospheric blocking, *Nature Geosci.*, **8**, 610 - 614.

Pomroy, H. R., and A. J. Thorpe, 2000: The evolution and dynamical role of reduced upper-tropospheric potential vorticity in intensive observing period one of FASTEX. *Mon. Wea. Rev.*, **128**, 1817–1834.

Protat A., J. Pelon, J. Testud, N. Grand, P. Delville, P. Laborie, J.-P. Vinson, D. Bouniol, D. Bruneau, H. Chepfer, J. Delanoe, M. Haeffelin, V. Noel, and C. Tinel, 2004: Le projet RALI : Combinaison d'un radar nuage et d'un lidar pour l'étude des nuages faiblement précipitants, La Météorologie, n° 47, 23-33.

Rabier F., P. Gauthier, C. Cardinali, R. Langland, M. Tsyrulnikov, A. Lorenc, P. Steinle, R. Gelaro, K. Koizumi, 2008: An update on THORPEX-related research in data assimilation and observing strategies. *Nonlinear Processes in Geophysics*, European Geosciences Union (EGU), **15**, 81-94.

Rautenhaus, M., G. Bauer, and A. Dörnbrack, 2012. A web service based tool to plan atmospheric research flights. *Geosci. Mod4el Dev.*, **5**, 55-71.

Rautenhaus, M., M. Kern, A. Schäfler, and R. Westermann, 2015a: Three-dimensional visualization of ensemble weather forecasts - Part 1: The visualization tool Met.3D (version 1.0). *Geosci. Model Dev.*, **8**, 2329-2353.

Rautenhaus, M., C. M. Grams, A. Schäfler, and R. Westermann, 2015b: Three-dimensional visualization of ensemble weather forecasts - Part 2: Forecasting warm conveyor belt situations for aircraft-based field campaigns. *Geosci. Model Dev.*, **8**, 2355-2377.

Reitebuch, O., C. Lemmerz, E. Nagel, U. Paffrath, Y. Durand, M. Endemann, F. Fabre, and M. Chaloupy, 2009: The airborne demonstrator for the direct-detection Doppler wind lidar ALADIN on ADM-Aeolus: I. Instrument design and comparison to satellite instrument. *J. Atmos. Oceanic Technol.*, **26,** 2501-2515.

Richardson, D., J. Bidlot, L. Ferranti, A. Ghelli, T. Haiden, T. Hewson, M. Janousek, F. Prates, and F. Vitart, 2012: Verification statistics and evaluations of ECMWF forecasts in 2011-2012. ECMWF Technical Memorandum, 688.

Riemer, M., and S. C. Jones, 2010: The downstream impact of tropical cyclones on a developing baroclinic wave in idealized scenarios of extratropical transition. *Quart. J. Roy. Meteor. Soc.*, **136,** 617-637.

Rodwell, M. J., and Co-authors, 2013: Characteristics of occasional poor medium-range weather forecasts for Europe. *Bull. Amer. Meteor. Soc.*, **94**, 1393-1405.

Schäfler, A., and F. Harnisch, 2015: Impact of the inflow moisture on the evolution of a warm conveyor belt. *Quart. J. Roy. Meteor. Soc*, **141**, 299–310. doi: 10.1002/qj.2360

Schäfler, A., M. Boettcher, C. M. Grams, M. Rautenhaus, H. Sodemann, and H. Wernli, 2014: Planning of aircraft measurements within a warm conveyor belt. *Weather*, **69**, 161–166. doi: 10.1002/wea.2245

Schwierz, C., S. Dirren, and H. C. Davies, 2004: Forced waves on a zonally aligned jet stream. *J. Atmos. Sci.*, **61**, 73–87.

Selz, T., and G. C. Craig, 2015: Upscale error growth in a high-resolution simulation of a summertime weather event over Europe. *Mon. Wea. Rev.*, **143,** 813-827.

Sodemann, H. and A. Stohl, 2013: Moisture origin and meridional transport in Atmospheric Rivers and their association with multiple cyclones, *Mon. Wea. Rev.*, **141**, 2850–2868,

Spensberger, C., and T. Spengler, 2014: A new look at deformation as a diagnostic for large-scale flow. *J. Atmos. Sci.*, **71**, 4221-4234.

Sprenger, M., G. Fragkoulidis, H. Binder, M. Croci-Maspoli, P. Graf, C. M. Grams, P. Knippertz, E. Madonna, S. Schemm, B. Skerlak, and H. Wernli, 2017: Global climatologies of Eulerian and Lagrangian flow features based on ERA-Interim reanalyses. *Bull. Amer. Meteor. Soc*., doi: 10.1175/BAMS-D-15-00299.1

Szunyogh, I., Z. Toth, R. E. Morss, S. J. Majumdar, B. J. Etherton, and C. H. Bishop, 2000: The effect of targeted dropsonde observations during the 1999 Winter Storm Reconnaissance Program. *Mon. Wea. Rev.*, **128**, 3520–3537.

Thorpe, A. J., 2004: Weather forecasting: A centenary perspective. *Weather*, **59**, 332–335.

Vaughan, G., and Co-authors, 2015: Cloud banding and winds in intense European cyclones: results from the DIAMET project. *Bull. Amer. Meteor. Soc.*, **96**, 249-265.

Weissmann, M., R. Busen, A. Dörnbrack, S. Rahm, and O. Reitebuch, 2005: Targeted observations with an airborne wind lidar. *J. Atmos. Oceanic Technol.,* **22,** 1706-1719.

Weissmann, M., F. Harnisch, C. Wu, P. Lin, Y. Ohta, K. Yamashita, Y. Kim, E. Jeon, T. Nakazawa, and S. Aberson, 2011: The Influence of Assimilating Dropsonde Data on Typhoon Track and Midlatitude Forecasts. *Mon. Wea. Rev*., **139**, 908–920, https://doi.org/10.1175/2010MWR3377.1

Wendisch, M., D. Müller, D. Schell, and J. Heintzenberg, 2001: An air-borne spectral albedometer with active horizontal stabilization. *J. Atmos. Oceanic Technol.*, **18**, 1856–1866

Wendisch, M., U. Pöschl, M. O. Andreae, L. A. T. Machado, R. Albrecht, H. Schlager, D. Rosenfeld, S. T. Martin, A. Abdelmonem, A. Afchine, A. Araujo, P. Artaxo, H. Aufmhoff,

H. M. J. Barbosa, S. Borrmann, R. Braga, B. Buchholz, M. A. Cecchini, A. Costa, J. Curtius, M. Dollner, M. Dorf, V. Dreiling, V. Ebert, A. Ehrlich, F. Ewald, G. Fisch, A. Fix, F. Frank, D. Fütterer, C. Heckl, F. Heidelberg, T. Hüneke, E. Jäkel, E. Järvinen, T. Jurkat, S. Kanter, U. Kästner, M. Kenntner, J. Kesselmeier, T. Klimach, M. Knecht, R. Kohl, T. Kölling, M. Krämer, M. Krüger, T. C. Krisna, J. V. Lavric, K. Longo, C. Mahnke, A. O. Manzi, B. Mayer, S. Mertes, A. Minikin, S. Molleker, S. Münch, B. Nillius, K. Pfeilsticker, C. Pöhlker, A.-E. Roiger, D. Rose, D. Rosenow, D. Sauer, M. Schnaiter, J. Schneider, C. Schulz, R. A. F. de Souza, A. Spanu, P. Stock, D. Vila, C. Voigt, A. Walser, D. Walter, R. Weigel, B. Weinzierl, F. Werner, M. A. Yamasoe, H. Ziereis, T. Zinner, M. Zöger, 2016: The ACRIDICON-CHUVA campaign: Studying tropical deep convective clouds and precipitation over Amazonia using the new German research aircraft HALO. *Bull. Am. Meteorol. Soc.*, **97**, 10, 1885-1908, http://dx.doi.org/10.1175/BAMS-D-14-00255

Wernli, H., and H. C. Davies, 1997: A Lagrangian-based analysis of extratropical cyclones. I. The method and some applications. *Quart. J. Roy. Meteor. Soc*, **123**, 467–489.

Wernli, H., 1997: A Lagrangian-based analysis of extratropical cyclones. II. A detailed case-study. *Quart. J. Roy. Meteor. Soc*, **123**, 1677–1706.

Wernli, H., and M. Sprenger, 2007: Identification and ERA15 climatology of potential vorticity streamers and cut-offs near the extratropical tropopause. *J. Atmos. Sci.*, **64**, 1569-1586.

Wirth, M., A. Fix, P. Mahnke, H. Schwarzer, F. Schrandt, and G. Ehret, 2009: The airborne multi-wavelength water vapor differential absorption lidar WALES: system design and performance. *Appl. Phys. B*, **96**, 201-213.

Witschas, B., S. Rahm, A. Dörnbrack, J. Wagner, and M. Rapp, 2017: Airborne wind lidar measurements of vertical and horizontal winds for the investigation of orographically induced gravity waves. *J. Atmos. Oceanic Technol*., doi: 10.1175/JTECH-D-17-0021.1.

Wulfmeyer, V., and Co-authors, 2011: The Convective and Orographically induced Precipitation Study (COPS): The scientific strategy, the field phase, and research highlights. *Quart. J. Roy. Meteor. Soc.*, **137**, 3–30.

Zhang, F., N. Bei, R. Rotunno, C. Snyder, and C. C. Epifanio, 2007: Mesoscale predictability of moist baroclinic waves: Convection-permitting experiments and multistage error growth dynamics. *J. Atmos. Sci.*, **64**, 3579-3594.

Sidebar 1: Active remote-sensing observations for future satellite missions Aeolus and EarthCARE. HALO and the SAFIRE and DLR Falcons were equipped with remote-sensing instruments that are specifically relevant for the future Earth Explorer satellite missions EarthCARE (Illingworth et al. 2015) and Aeolus (ESA 2018) of the European Space Agency (ESA). NAWDEX observations, through coordinated flights of multiple aircraft and of aircraft with satellite overpasses, provide data from comparable airborne instruments for the preparation and future validation of these satellite instruments.

HALO was equipped with the High Spectral Resolution (HSRL, 532 nm) and water vapor Differential Absorption Lidar (DIAL) WALES, the HALO Microwave Package (HAMP) with a 35.2 GHz cloud radar and microwave radiometers, the cloud spectrometer (specMACS) and the visible to near-infrared SMART instrument (Table 2). The French Falcon was also equipped with the RAdar-LIdar (RALI, Protat et al. 2004) payload consisting of the 94 GHz cloud radar RASTA and the UV High Spectral Resolution lidar LNG (Table 2). These aircraft provide the most complete instrumentation package available at the European level to mimic upcoming EarthCARE measurements and thus provide valuable data for preparing the EarthCARE mission and for future validation. Coordinated flights with both aircraft as well as CALIPSO-Cloudsat underpasses during NAWDEX delivered independent measurements for testing EarthCARE L2 algorithms at different wavelengths and for performing a first rehearsal of the validation/calibration for EarthCARE.

Figure SB1 (a) illustrates the complementary character of lidar and radar measurements taken during the HALO research flight on 1 October 2016. Optically thin ice clouds at cloud top are only visible in the lidar measurements (green marked curtain), while optically thicker cloud regions are only visible in cloud radar measurements (red marked curtain).

The DLR Falcon was equipped with a Doppler wind lidar (DWL) payload consisting of the A2D direct-detection DWL and a 2-µm scanning coherent/heterodyne detection DWL. The A2D is the prototype of the satellite-borne wind lidar instrument on Aeolus and provides range-resolved line of sight wind speeds with high data coverage by exploiting both molecular and particulate backscatter return. With a view to the pre-launch activities for the upcoming Aeolus mission, NAWDEX offered the opportunity to extend the A2D dataset and to perform wind measurements in dynamically complex scenes, including strong wind shear and varying cloud conditions, as well as multiple instrument calibrations, which are a prerequisite for accurate wind retrieval. RALI on board the SAFIRE Falcon complemented the A2D instrument with wind measurements in clouds and aerosol-rich layers.

Figure SB1 (b) shows collocated wind observations from the A2D and the 2-µm DWL from a flight of the DLR Falcon east of Iceland on 4 October 2016. The good vertical coverage, limited only by a dense cloud layer is achieved by combining complementary information from both aerosol backscatter (A2D Mie channel and 2-µm DWL) and molecular backscatter (A2D Rayleigh channel).

Sidebar 2: Forecast products to investigate forecast uncertainty. NAWDEX focused on weather phenomena that are poorly represented in NWP, so a strong effort to estimate forecast uncertainty was essential for the planning of the IOPs. Deterministic forecasts from the European Centre for Medium-Range Weather Forecasts (ECMWF), the UK Met Office, the Naval Research Laboratory (NRL), Météo France, the Icelandic Meteorological Office (IMO) and the Danish Meteorological Institute (DMI) were available. Additionally, ensemble forecasts from the ECMWF, Met Office (MOGREPS-G) and Météo France (PEARP short-range ensemble) played an essential role.

Each day a standard set of synoptic charts and tailored weather products (e.g. PV on isentropic surfaces and WCB trajectories) were produced using a common map projection and pre-defined cross sections. Ensemble diagnostics of mean and spread of several variables, as well as tailored ensemble forecast products for NAWDEX-relevant features (e.g., WCB and cyclone frequencies, and tropopause height) were created. These forecast products were provided via web sites. In addition, an interactive web interface allowed the flight planning team to compute backward and forward trajectories from planned flight tracks, facilitating the planning of flights to attempt Lagrangian re-sampling of air masses.

Flight planning typically requires cross-section information, e.g., to obtain an accurate picture of tropopause height, winds speeds and cloud layers, and to assess forecast uncertainties along hypothetical flight routes. The NAWDEX community had access to special flight planning tools that allowed an interactive visualization of forecast products. Central to forecasting and flight planning operations was the "Mission Support System" (MSS; Rautenhaus et al. 2012). In addition, the interactive 3D forecast tool "Met.3D" (Rautenhaus et al. 2015a) provided specialized forecast products. Two workstations were set up at the operation center in Keflavik to run Met.3D and enable the novel ensemble forecasting workflow described in Rautenhaus et al. (2015b). Ensemble forecasts by ECMWF could be interactively analyzed in combined 2D/3D depictions. WCB trajectories and derived probabilities of WCB occurrence could be combined with additional forecast information. The ability of Met.3D to interactively navigate the ensemble data proved particularly useful, facilitating analysis of the uncertainty for features such as the predicted tropopause position.

Figure SB2 shows an example of forecast products used for planning the IOP4 flight. The +60 h deterministic IFS forecast shows ex-TS Karl as deep surface cyclone south of Greenland (Fig. SB2a) with cyclonically-wrapped PV contours resulting from an advection of low-PV air to upper levels in the outflow of a WCB. High WCB probabilities with two distinct maxima north and east of Karl indicate that the location of the tropopause and WCB outflow is predicted with high certainty (Fig. SB2b). Images from Met.3D (Fig. SB2c,d) show the relation between the jet stream, WCB and tropopause in the ECMWF ensemble mean along cross sections intersecting the waveguide and the WCB east of the surface cyclone. A cross section with ensemble mean PV (Fig. SB2c) shows a low tropopause north of the jet (depicted by an isosurface of wind speed), whereas a high tropopause appears to the south. This coincides with high probabilities of WCB outflow (Fig. SB2d). WCB trajectories of a selected ensemble member show two distinct branches (Fig. SB2d); one branch wraps cyclonically around the cyclone and features a lower outflow compared to the second branch, that follows anticyclonic pathways at higher elevations, contributing to the WCB probability maximum there. Real-time adjoint products from COAMPS (Doyle et al. 2014) were used to identify regions of initial condition sensitivity. At 12 UTC 24 September, the maximum moisture sensitivity is located in the low- to mid-levels and positioned along the eastern portion of TS Karl (Fig. SB2e). The adjoint sensitivity is computed using a kinetic energy response function located in a box (450 x 600 km^2 in the horizontal and extending from the surface to 700 hPa) centered on the ascending WCB at the 48 h forecast time at 12 UTC 26 September when the IOP4 flights were planned. Optimal perturbations derived from the adjoint sensitivity show an increase of wind speeds from 30 m s^{-1} to over 45 m s^{-1} in the WCB highlighting the importance of the mid-level moisture associated with Karl (48 h prior) for the intensification of the WCB.

Table 1: NAWDEX research topics and science goals. Region numbers refer to Fig. 1

Aim Nr	**Topic**	**Science Goals**	**Region**
1	Moisture structure in the boundary layer	• Characterization of low-level moisture in atmospheric rivers and WCB inflow regions • Investigation of impact of low-level moisture on downstream weather evolution	1,(2,3),4
2	Mixed phase and cirrus clouds	• In-situ and remote sensing measurements of cloud properties and meteorological parameters during WCB ascent and outflow • Comparison of observations and models to quantify latent and radiative heating/cooling in and below WCB • Role of slantwise ascent vs. embedded convection in WCB • Characterization of vertical moisture gradient and cirrus structure in WCB outflow, and effects on radiation	2, 3
3	Potential vorticity	• Quantitative estimate of PV from observations • Verification of PV structures, PV gradients and jet stream winds in numerical models • Structure of negative PV anomalies in WCB outflows and upper tropospheric ridges • Role of divergent outflow of WCBs for ridge amplification • Spatial distribution of turbulence in the free atmosphere and relationship to jet stream and PV structures	3
4	Tropopause waveguide, predictabilty and HIW	• Relevance of amplifying small errors at tropopause level for uncertainty in surface weather downstream • Influence of observations within and outside of diabatically-active regions on the predictability of downstream HIW	3, 4
5	Instrument-driven aims	• Comparison of measured radiances and retrieved cloud optical properties between SMART-HALO and specMACS • Cloud regime characterization in mid-latitude cyclones and analysis of model representation at different resolutions • Radiometer retrieval development for profiles and hydrometeor paths using instrument synergies • Validation of Aeolus calibration and wind retrieval algorithms • Intercomparison of wind and aerosol products from different instruments on DLR and SAFIRE Falcon • First test of EarthCARE calibration and validation strategy	2,3

Table 2: Aircraft and instrumentation for NAWDEX		
Aircraft	**Instruments**	**Measured and derived properties**
HALO	**HAMP** (HALO Microwave Package) microwave radiometer with 26 channels spanning the frequency range from 22 to 183 GHz, and Ka-band (35.2 GHz) cloud radar (Mech et al. 2014)	Radiometers: Integrated water vapor, temperature and humidity profiles, liquid and ice water path Radar: profiles of radar reflectivity, depolarization ratio, vertical velocity
	WALES (Water Vapor Lidar Experiment in Space): Four-wavelength Differential Absorption (DIAL) and High Spectral Resolution Lidar (HSRL) (Wirth et al. 2009)	Profiles of water vapor, backscatter coefficient lidar/color ratio, particle linear depolarization ratio, particle extinction coefficient
	SMART (Spectral Modular Airborne Radiation Measurement System): Passive cloud spectrometer (Wendisch et al., 2001; Ehrlich et al., 2008)	Spectral nadir radiance, spectral upward and downward irradiance (300-2200 nm), cloud top albedo, cloud thermodynamic phase, cloud optical thickness, effective radius, cloud cover / statistics
	specMACS (Cloud spectrometer of the Munich Aerosol Cloud Scanner): Imaging cloud spectrometer plus 2D RGB camera (+/-35° fov) (Ewald et al. 2015)	Spectral radiance (400-2500 nm), push-broom imaging at nadir and +/- 17° across track, cloud thermodynamic phase, liquid and ice optical thickness, particle size, cloud cover
	Bahamas (Basic HALO Measurements and Sensor System)	In-situ observations of pressure, temperature, wind, humidity, TAS aircraft position, attitude, heading, altitude
	Dropsondes Vaisala RD94	Temperature, humidity and wind profiles
DLR Falcon	**A2D** (ALADIN Airborne demonstrator): direct-detection DWL (Reitebuch et al. 2009, Marksteiner et al. 2011)	Profiles of line of sight wind speed and aerosol/cloud layers(20° off-nadir)
	2-µm scanning coherent/heterodyne detection DWL (Weissmann et al. 2005; Witschas et al. 2017)	Vertical profiles of line of sight wind speed, horizontal wind vectors, and aerosol/cloud layers
	Basic in-situ measurements	In-situ observations of pressure, temperature, wind, humidity, TAS aircraft position, attitude, heading, altitude
SAFIRE Falcon	**RASTA** (RAdar SysTem Airborne): 95-GHz Doppler cloud radar (Delanoë et al 2013)	Doppler velocity and reflectivity from three antennas (including spectral width), cloud and precipitation microphysics (ice and liquid water content), dynamics (horizontal and vertical wind)
	LNG (Leandre New Generation): high-spectral-resolution lidar (Bruneau et al. 2015)	Three-wavelength (1064, 532, and 355 nm) backscatter lidar with polarization analysis at 355 nm, High Spectral Resolution capability including Doppler measurement, based on a Mach–Zehnder Interferometer, at 355 nm. Radiative properties and dynamics of cloud and aerosol
	CLIMAT infrared radiometer (Brogniez et al. 2003)	Radiances measured simultaneously in three narrowband channels centered at 8.7, 10.8, and 12.0 micron

	Dropsondes Vaisala RD94	Temperature, humidity and wind profiles
	Aircraft in-situ measurements	In-situ observations of pressure, temperature, wind, humidity, TAS aircraft position, attitude, heading, altitude
FAAM BAe 146 (Payload as in Vaughan et al. 2015)	In-situ temperature, Buck CR-2 and WVSS-2 hygrometers, two turbulence probes	Temperature, humidity, and wind and turbulent fluxes
	PCASP (aerosol size probe), CDP (scattering cloud droplet probe), CIP-15, CIP-100 (cloud imaging probes)	Cloud particle size spectrum: 2 μm-6 mm diameter, cloud droplet spectrum: 3-50 μm
	Nevzorov hot wire probe	Ice/Liquid water content
	TECO 49C UV analyser, Aerolaser AL5002, Los Gatos Fast Greenhouse Gas analyser	O3, CO, CH4,CO2
	Lidar: downward-pointing Leosphere ALS450 (355 nm, scattering and depolarization)	Position of different atmospheric layers below the aircraft (clear air, aerosols, cloud tops)
	ISMAR (International Sub-Millimetre Airborne Radiometer)	Passive radiometer with polarisation and multiple channels (118, 243 (V/H), 325, 424, 448, 664 (V/H) and 874 GHz (V/H)) (IOP11 only)
	MARSS (Microwave Airborne Radiometer Scanning System)	Scanning microwave radiometer operating at AMSU-B channels 16-20 (89-183GHz) and pointing both upward and downward (IOP11 only)
	Dropsondes Vaisala RD94	Temperature, humidity and wind profiles

940

Table 3: IOPs, key weather systems and associated flights together with the number of dropsondes from all aircraft. As some of the long-range flights of HALO were related to different weather systems, dropsondes were assigned to the respective IOP. Aims numbered according to Table 1 show contribution to NAWDEX science goals.

IOP	Period	Key Weather systems	Date	HALO	DLR Falcon	SAFIRE Falcon	FAAM BAe 146	Drops	Aim Nr
1	16-17 Sep	Outflow of ex-TC **Ian**, low predictability case	17 Sep	RF01	RF01/02			10	2,3,4,5
2	21-22 Sep	WCB ascent and outflow of extratropical cyclone **Ursula**	21 Sep	RF02	RF03			14	2,3,4,5
3	23-25 Sep	WCB ascent of extratropical cyclone **Vladiana**	23 Sep	RF03	RF04		RF01 (B980)	32	1,2,3,4,5
4	22-28 Sep	Re-intensification phase of ex-TS **Karl & jet streak** forming downstream	26 Sep	RF04				25	2,3,4,5
			27 Sep	RF05	RF05		RF02 (B981)	22	
5	26-29 Sep	Strong WV transport of extratropical cylone **Walpurga** leading to HIW in Scandinavia	27 Sep	RF05				20	1,3,4
6	1-5 Oct	**”Stalactite Cyclone”** and low predictability over Europe	1 Oct	RF06		RF05		3	2,3,4,5
			2 Oct		RF07	RF06/07		9	
7	4-5 Oct	Strong extratropical cyclone originating as frontal wave near Newfoundland	4 Oct		RF08/09	RF08		5	
			5 Oct			RF09		4	2,3,4
8	6-9 Oct	**TPV** near Newfoundland and downstream forming cyclone	6 Oct	RF07				20	4,5
			7 Oct			RF10		7	
			9 Oct	RF08	RF10	RF11/12		9	
			10 Oct			RF13		6	
9	9-14 Oct	PV cut-off cyclone **“Sanchez”**& downstream impact over the Mediterranean	9 Oct	RF08					2,3,4,5
			10 Oct	RF09				20	
10	12-15 Oct	Formation and extension of tropopause ridge **“Thor” and the Scandinavian anticyclone**	11 Oct			RF14		4	3,4,5
			12 Oct			RF15		8	
			13 Oct	RF10		RF16		26	
			15 Oct	RF12				12	
11	14 Oct	Radar and lidar mission for instrument comparisons and satellite underflights	14 Oct	RF11		RF17/18	RF03 (B984)	15	5
12	15 Oct	**TPV** over Baffin Island	15 Oct	RF12					4, 5
13	18 Oct	PV streamer over UK	18 Oct	RF13	RF13/14			16	2,3
		Instrument and calibration flights	28 Sep		RF06				5
			15 Oct		RF11/12				
			16 Oct			RF19		2	
			22 Oct		RF15/16				

Table 4: NAWDEX IOPs and periods of increased ground-based observation activities.

IOP	Additional Observations	Period
IOP1	Radiosondes from UK, Torshavn and Iceland for a temporal sequence of the arrival of outflow of ex-TC Ian as it extends northeastwards	16-17 Sep
IOP2	Radiosondes from UK, Iceland and eastern Greenland for a time series during arrival and passage of cyclone Ursula	21-22 Sep
IOP3	Radiosondes from northern UK to observe rapidly intensifying frontal cyclone Vladiana with strong WCB and ridge building	23-25 Sep
IOP4	Radiosondes around the northern North Atlantic and Scandinavia to observe the structure and evolution of ex-TS Karl and to observe GWs above Iceland at the jet stream. Jet streak maximum passes directly above MST radar wind profiler on South Uist, Scotland	26-28 Sep
IOP5	Radiosondes in UK and southern Scandinavia to observe the strong water vapor transport and related HIW. Passage of jet stream over Capel Dewi.	27-29 Sep
IOP6	Radiosondes northwest of Iceland to observe ridge building in relation to „Stalactite Cyclone“. Radiosondes over Southern Europe to observe a cut-off downstream of the „Stalactite Cyclone“. Radiosondes at Iceland to observe GWs in the stratosphere.	1-5 Oct
IOP8	Radiosondes over Iceland and eastern Greenland to observe WCB ascent and cyclone structure. Observation of orographic GWs above Iceland.	6-9 Oct
IOP9	Radiosondes from the western Mediterranean, at Capel Dewi and at SIRTA to observe cut-off “Sanchez” and related HIW. Passage of outflow from Sanchez over MST radar at Capel Dewi. Radiosondes above Iceland to observe strong GW activity in the stratosphere.	10-14 Oct
IOP8,IOP10	Radiosondes over North Atlantic to obtain a time series of the vertical structure of the ridge “Thor”, MST radar wind observations at Andøya , Norway	10-15 Oct
IOP11	Radiosondes at SIRTA to observe the downstream impact	15-16 Oct

Table 5: NAWDEX observational highlights

IOP and period	**Specific aspects of the observations**
IOP3 23-25 Sep	Coordinated flights to observe the cloud structure and cloud physics in the WCB ascent related to cyclone Vladiana and the interaction of the WCB outflow with the jet stream.
IOP4 22-28 Sep	First ever observations of a TS followed from tropical phase and ET (SHOUT observations) to a mid-altitude re-intensification, jet streak formation, ridge enhancement and HIW over Scandinavia (NAWDEX observations)
IOP5 26-29 Sep	Large-scale strong moisture transport in an atmospheric river type flow upstream of a cyclone causing HIW over Scandinavia
IOP6 1-5 Oct	Lowest predictability case with observation of the WCB ascent and outflow of the so-called “stalactite cyclone” and the subsequent influence in the onset of the European block.
IOP8/IOP12 26-29 Sep / 15 Oct	First ever airborne observation of temperature, wind and moisture structure of two TPV events in a phase when they interacted with the mid-latitude waveguide
IOP9 9-14 Oct	Roll-up of the positive PV filament giving rise to mesocyclone “Sanchez” connected to HIW in France and Italy
IOP10 12-15 Oct	Low PV ridge builds and extends into the Arctic reinforcing the anticyclonic part of the block.
IOP11 14 Oct	Coordination of three aircraft and joint underflight of the Calipso/Cloudsat satellite path to exploit instrument synergies of radar, lidar and radiometer instruments

Table A1. Overview of the NAWDEX team members and their roles.

Organization	Country	Participants	Role
Monash University	Australia	Julian Quinting	Flight Planning Team
Environment and Climate Change Canada (ECCC)	Canada	Ron McTaggart-Cowan	PI Canadian radiosondes, Science Team
Division Technique, INDU	France	Frédéric Blouzon	RALI Team
Institut Pierre Simon Laplace	France	Jean-Charles Dupont	Coordinator of radiosonde launches at SIRTA
Laboratoire d'Aérologie	France	Jean-Pierre Chaboureau	Flight Planning Team
Laboratoire de Météorologie Dynamique	France	Gwendal Rivière	Science Team, Flight Planning Team
Météo France	France	Philippe Arbogast Jean-Marie Donier	Science Team, Flight Planning Team UHF radar at Lannion (France)
SAFIRE	France	Roman Attinger, Hanin Binder, Maxi Boettcher, Bas Crezee, Christian Grams, Jacopo Riboldi	Flight Planning Team
Deutsches Zentrum für Luft- und Raumfahrt (DLR), Flight Experiments	Germany	Andreas Minikin, Robert Uebelacker, Katrin Witte	HALO and Falcon project management
		Stefan Hempe, Frank Probst	HALO and Falcon operations
		Steffen Gemsa, Michael Grossrubatscher, Stefan Grillenbeck, Philipp Weber, Roland Welser, Matthias Wiese	HALO and Falcon pilots
		Volker Dreiling, Andreas Giez, Christian Mallaun, Martin Zöger	HALO and Falcon Sensor and Data Team
		Michael Kettenberger, Thomas Leder, Florian Gebhardt, Christoph Grad, Stephan Storhas, David Woudsma	HALO technical support
Deutsches Zentrum für Luft- und Raumfahrt	Germany	Andreas Schäfler	Mission coordinator, Flight Planning Team
		Axel Amediek, Andreas Fix, Silke Groß, Manuel Gutleben,	WALES Team

(DLR), Institute for Atmospheric Physics		Martin Wirth	
		Christian Lemmerz, Oliver Lux, Uwe Marksteiner, Engelbert Nagel, Stephan Rahm, Oliver Reitebuch, Benjamin Witschas	Wind Lidar Team
		Florian Ewald, Martin Hagen	HAMP operations
		Martina Bramberger, Alenka Senika	Radiosonde Team at Keflavik, Flight Planning Team
Karlsruhe Institute of Technology	Germany	Pila Bossmann, Enrico Di Muzio, Florian Pantillion	Flight Planning Team
Max Planck Institute for Meteorology (MPI-M) Hamburg	Germany	Björn Brügmann, David Hellmann, Lutz Hirsch, Friedhelm Jansen, Marcus Klingebiel	HAMP radar operations
Technical University Munich	Germany	Marc Rautenhaus	Flight Planning Team
University of Cologne	Germany	Mario Mech, Susanne Crewell, Marek Jacob, Lisa Dirks	HAMP radiometer operations
University of Hamburg, Max Planck Institute for Meteorology (MPI-M)	Germany	Felix Ament, Heike Konow	HAMP radar and radiometer operations
University of Leipzig	Germany	Kevin Wolf, Tim Carlsen, André Ehrlich, Manfred Wendisch	SMART operations
University of Mainz	Germany	Marlene Baumgart, Christian Euler, Paolo Ghinassi, Michael Riemer, Volkmar Wirth	Flight Planning Team
University of Munich	Germany	George Craig	HALO Mission PI, Science Team, Flight Planning Team
		Florian Baur, Lotte Bierdel, Christian Keil, Julia Mack, Tobias Selz	Flight Planning Team
		Hans Grob, Lucas Höppler, Tobias Kölling, Bernhard Mayer, Tobias Zinner	specMACS operations
Norwegian Meteorological Institute	Norway	Rich Moore	NEAREX Team
University of	Norway	Thomas Spengler,	NEAREX Team

Bergen		Harald Sodemann	
National Institute of Research and Development for Optoelectronics	Romania	Dragos Ene	Flight Planning Team
ETH Zurich	Switzerland	Heini Wernli	Science Team, Flight Planning Team
		Roman Attinger, Hanin Binder, Maxi Boettcher, Bas Crezee, Christian Grams, Jacopo Riboldi	Flight Planning Team
University of Bern	Switzerland	Matthias Röthlisberger	Flight Planning Team
Met Office	UK	Richard Cotton, Stuart Fox	FAAM aircraft
NCAS and University of Manchester	UK	Geraint Vaughan Hugo Ricketts Bogdan Antonescu	Capel Dewi observations, FAAM aircraft
University of Reading and NCAS	UK	John Methven, Suzanne Gray	FAAM aircraft, NAWDEX-Influence PIs, Science Team, Flight Planning Team
		Ben Harvey, Jacob Maddison, Leo Saffin, Oscar Martínez-Avarado	Flight Planning Team
Naval Research Laboratory Monterey Washington, DC	USA	Jim Doyle	Science Team, Flight Planning Team
		Carolyn Reynolds Stephen Eckermann	Flight Planning Team Flight Planning Team
EUMETNET		Susanne Hafner, Stefan Klink	EUMETNET coordinators
ESA		Dirk Schüttemeyer	ESA campaign section

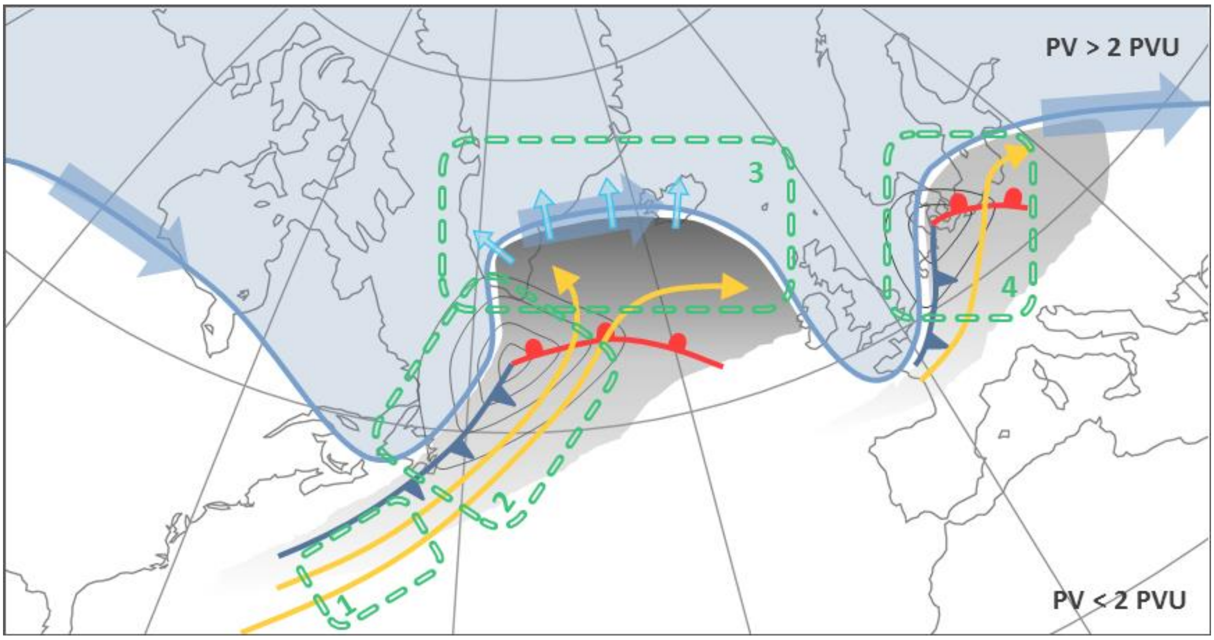

Fig. 1. Schematic of an idealized weather situation during NAWDEX. The blue line marks the location of the waveguide with a strong isentropic PV gradient separating stratospheric (blue background, PV > 2 PVU) from tropospheric air (white background). The jet stream (dark blue arrows) follows the waveguide. Surface lows develop below the leading edge of upper-level positive PV anomalies (black lines indicate sea level pressure and dark blue and red lines surface cold and warm fronts, respectively). Grey shaded areas indicate clouds related to ascending WCBs (yellow arrows). Light blue arrows mark divergent outflow at the tropopause. The four green boxes outline the main areas of interest, i.e., the inflow (1), ascent (2) and outflow (3) of WCBs, as well as a region of expected downstream impact (4).

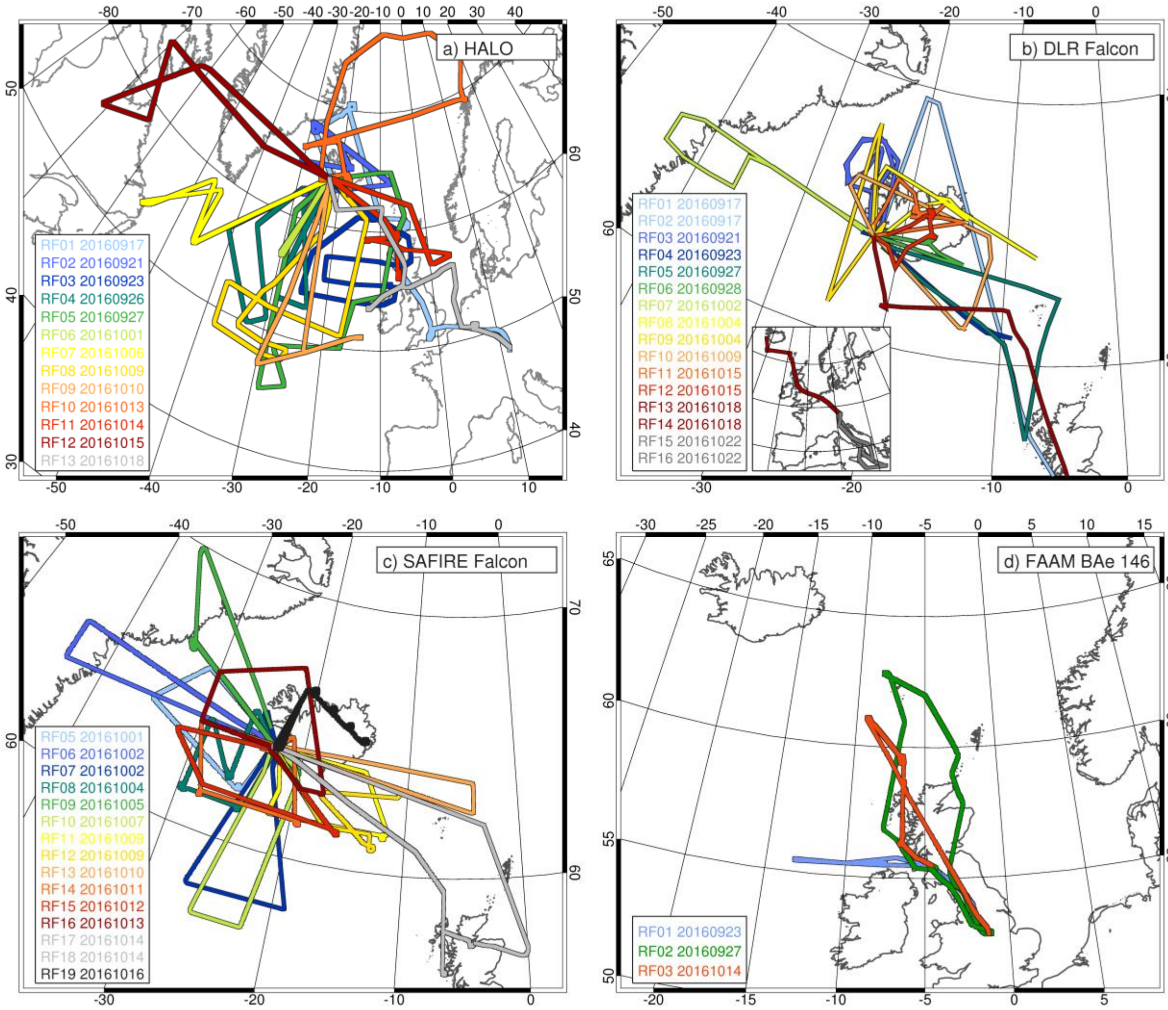

Fig. 2. Tracks of consecutively numbered research flights (RFs) of (a) HALO (97 flight hours during 13 RFs), (b) DLR Falcon (51 flight hours during 16 RFs) (c) SAFIRE Falcon (42 flight hours during 14 RFs), and (d) FAAM BAe 146 (15 flight hours during 3 RFs).

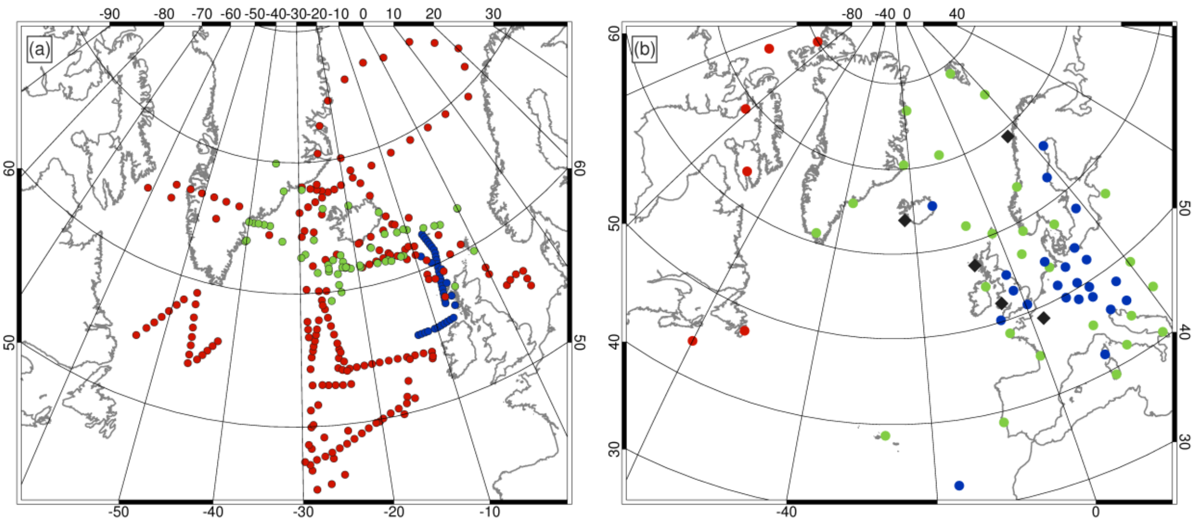

Fig. 3. (a) Dropsondes launched from HALO (red dots, 191 dropsondes), SAFIRE Falcon (green dots, 59 dropsondes) and FAAM BAe 146 (blue dots, 39 dropsondes). (b) Ground-based observation sites during NAWDEX: Canadian radiosonde stations (red dots), European radiosonde stations that performed only operational ascents (blue dots) and those with additional radiosonde launches (green dots), and five sites with additional profile observations (black diamonds).

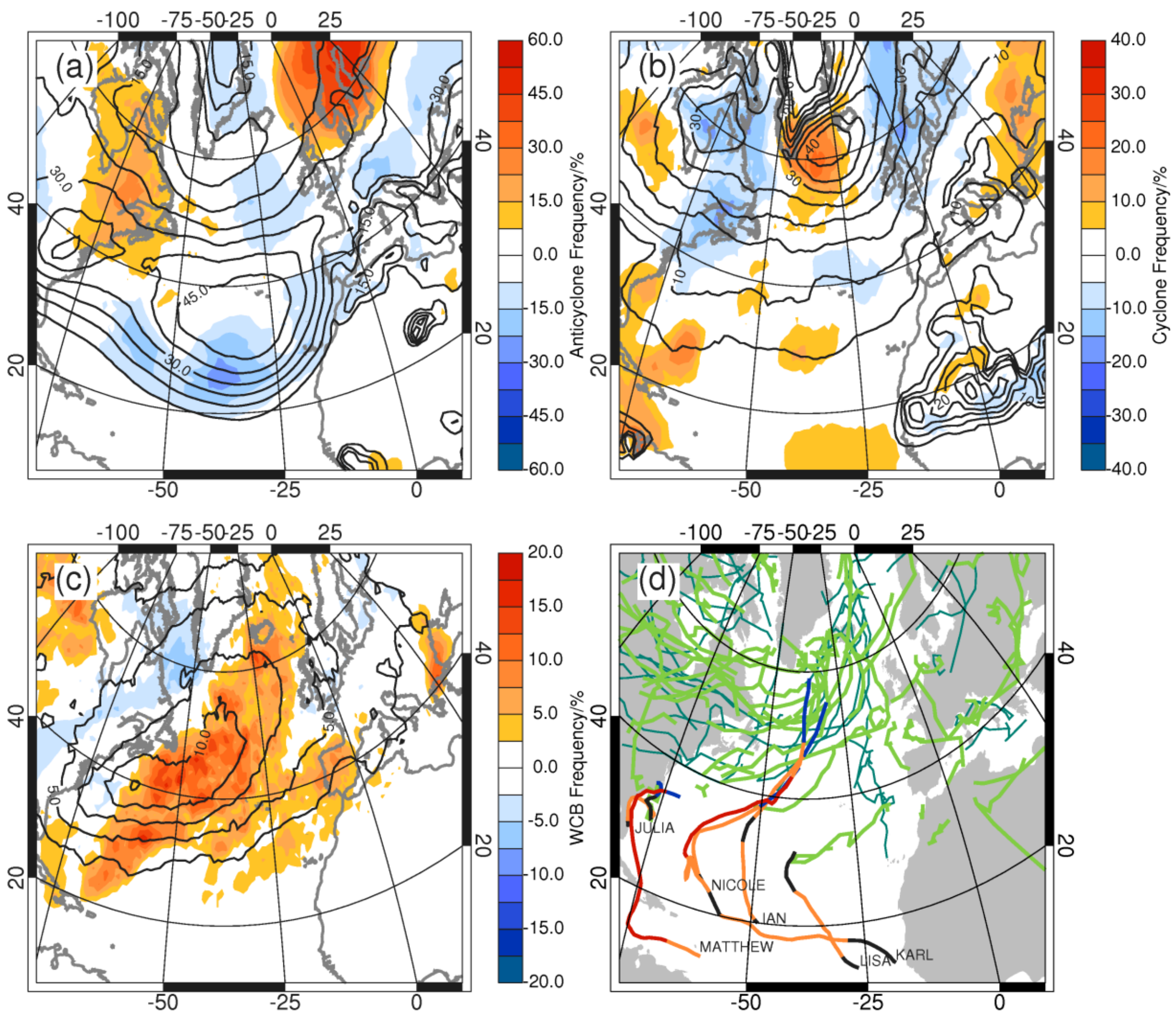

Fig. 4. (a-c) Synoptic-scale conditions during NAWDEX. All panels are based on ECMWF ERA-Interim data (1979-2016) and show in colors deviations of the campaign period in 2016 from the mid Sept to mid Oct climatology. (a-c) frequencies (all in %) of (a) surface anticyclones, (b) surface cyclones, and (c) WCB, as in Sprenger et al. (2017). Black contours show the 37-year climatological mean; (d) best track data (HURDAT2 of the National Hurricane Center) of six tropical cyclones (red sections classified as hurricane, orange as TS and blue as extratropical storm), and cyclone tracks during the NAWDEX period (light green lines) and before/after the campaign period (dark green lines).

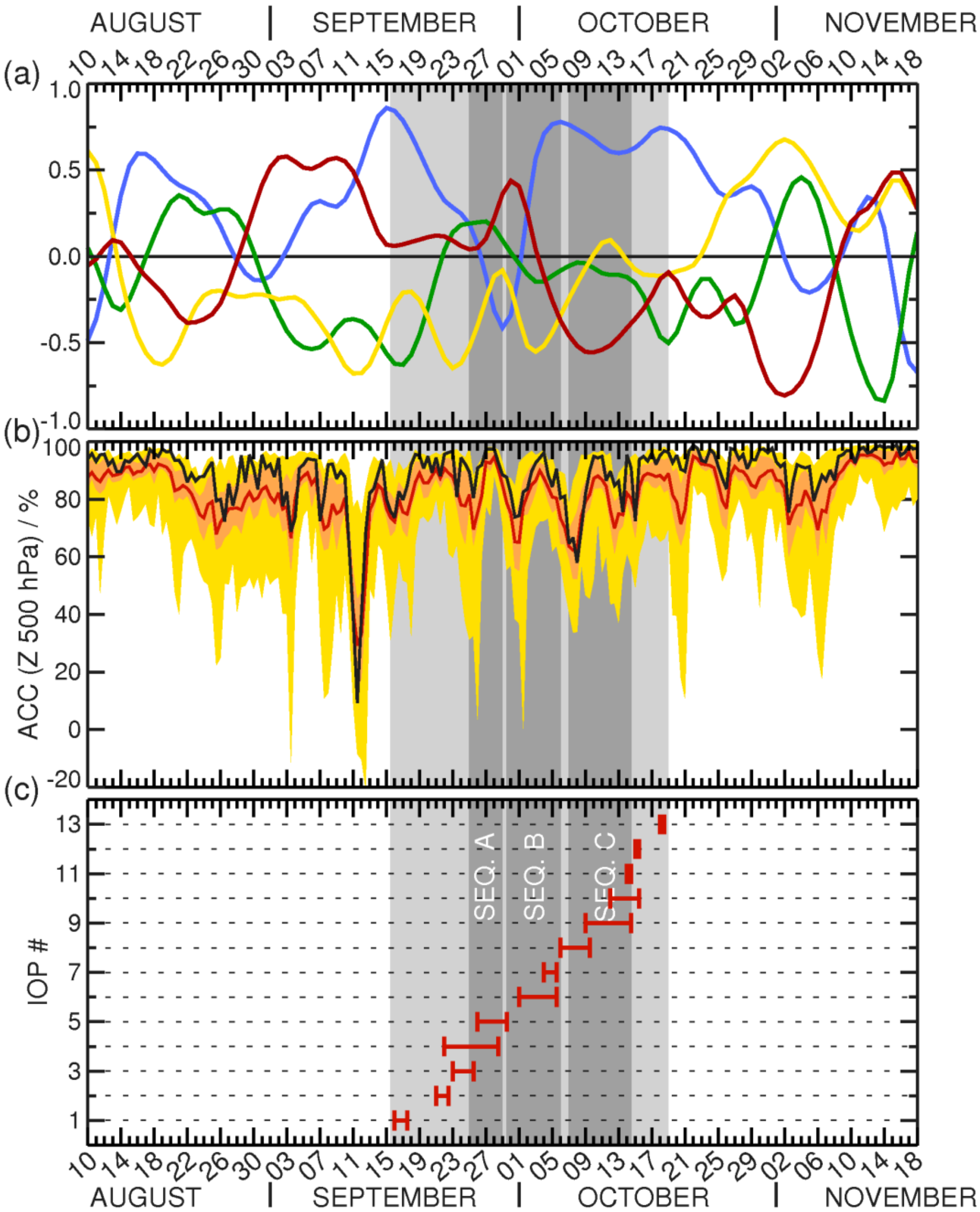

Fig. 5. (a) Weather regimes during NAWDEX: Scandinavian blocking (blue line), positive NAO (red line), negative NAO (green line), and Atlantic ridge (yellow line), identified with a k-means clustering approach (Michelangeli et al. 1995; Michel and Rivière 2011). (b) Time series of ECMWF IFS anomaly correlation coefficient (ACC) for geopotential height at 500 hPa over an area 35 to 75°N and 60 to 0°W for a forecast lead time of +120 h: IFS deterministic forecast (black line), ensemble mean (red line), 50% of the ensemble members (orange area) and all members (yellow area). (c) NAWDEX IOPs as indicated in Table 3. Grey boxes mark duration of weather sequences shown in Figure 6.

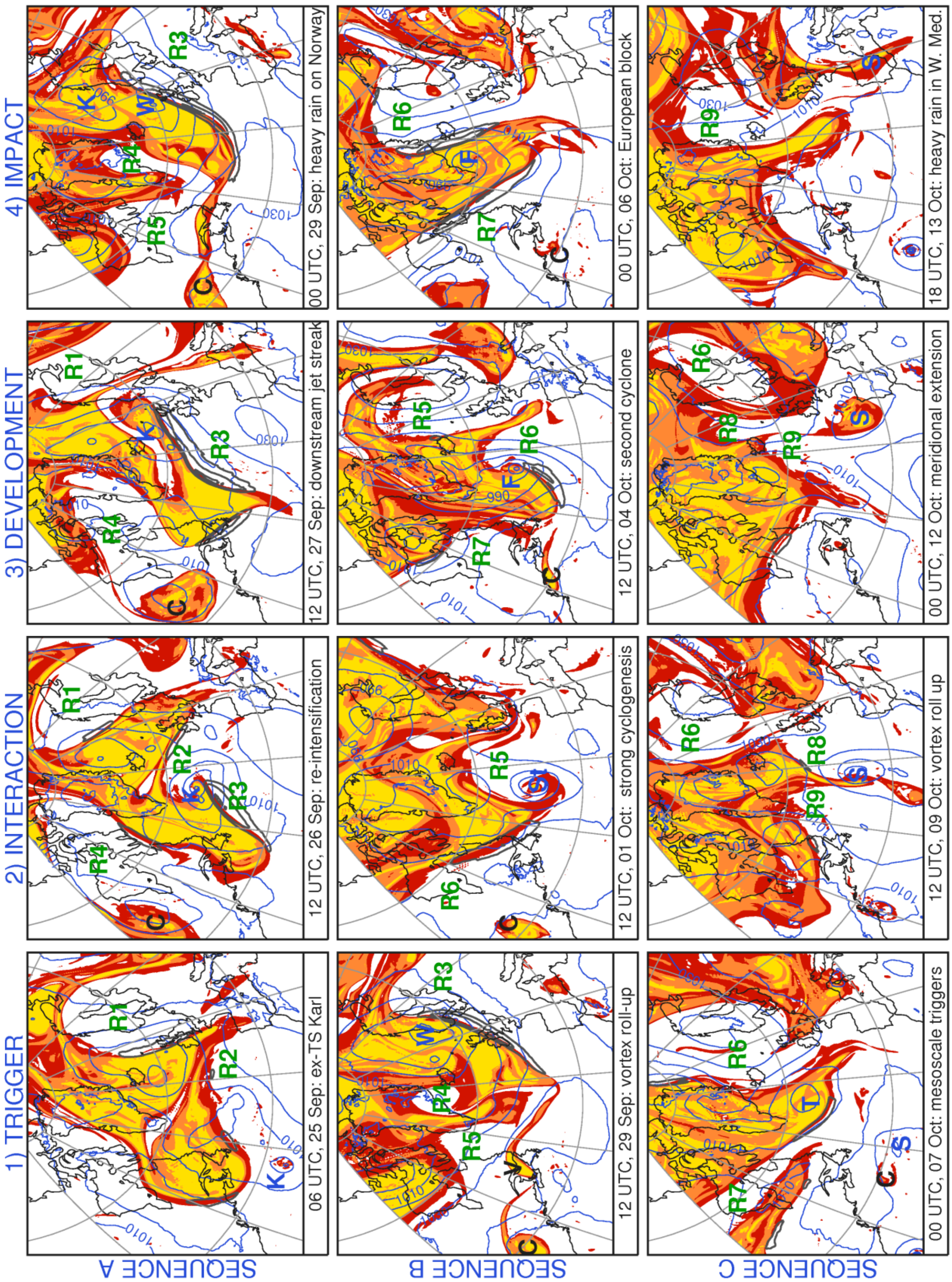

Fig. 6. Three sequences that illustrate the NAWDEX storyline from trigger to interaction, downstream development and HIW in Europe. All panels display PV on 325 K (PV < 2 PVU in white, 2 PVU ≥ PV < 5 PVU in red, 5 PVU ≥ PV < 8 PVU in orange, PV ≥ 8 PVU in yellow), contours of wind speeds (60, 70 and 80 m s^{-1}) and MSLP (blue contours; interval 10

hPa). Some long-lived, coherent features are labelled to enable links from one frame to the next. K refers to TS Karl; W, F, S and St mark mid-latitude cyclones observed by NAWDEX; C labels a tropopause level cut-off that persists for 10 days; R1-R9 refer to the prominent ridges along the North Atlantic waveguide, identified as northward excursions of the jet stream and the isentropic PV gradient; T marks a TPV.

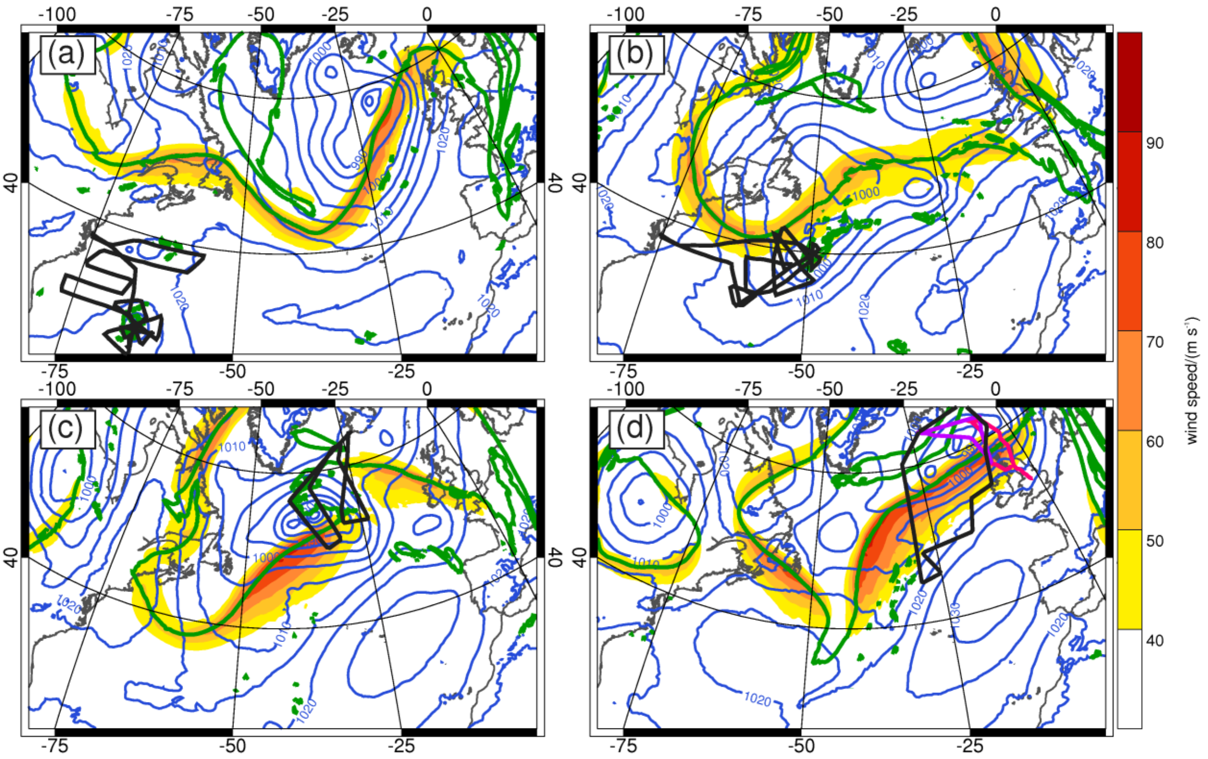

Fig. 7. Wind speed (color shading) and 2 PVU (green line) at 325 K and MSLP (blue contours, in hPa) at (a) 12 UTC 23 Sep 2016 with Global Hawk flight track (black line, from 2120 UTC 22 Sep to 2100 UTC 23 Sep), (b) 12 UTC 25 Sep 2016 with Global Hawk flight track (black line, from 1820 UTC 24 Sep to 1715 UTC 25 Sep), (c) 12 UTC 26 Sep 2016 with HALO flight track (black line, from 10 to 19 UTC), and (d) 12 UTC 27 Sep 2016 with HALO (black line, 1130 to 2030 UTC), FAAM (pink line, 0800 to 1230 UTC) and DLR Falcon (purple line, 0930 to 1330 UTC) flight tracks.

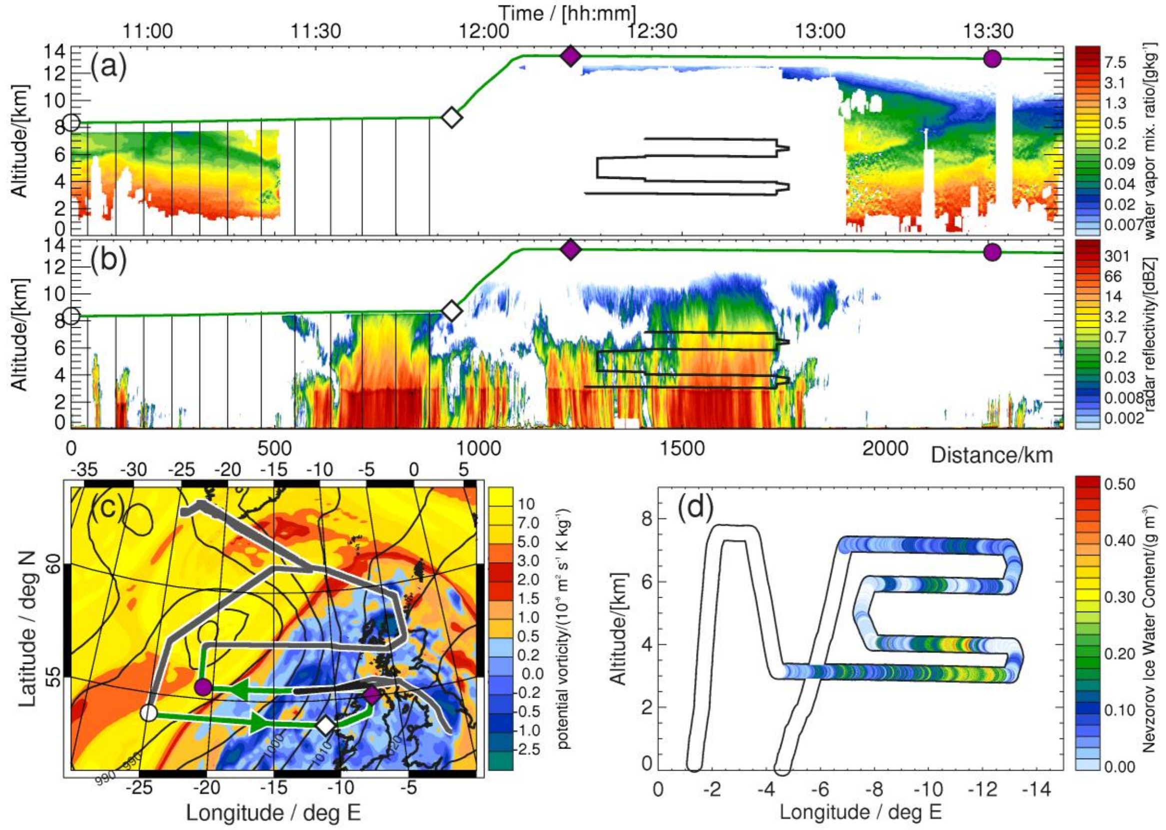

Fig. 8. WCB observations on 23 September 2016 (IOP3): (a) WALES DIAL water vapor mixing ratio (colors) and (b) HAMP radar reflectivity with HALO flight track (green line), FAAM flight track (thick black line, lowest leg was flown first) and dropsonde release positions (thin black lines). Only the part of the FAAM flight track with a spatial collocation to HALO is shown and both aircraft started at the same time, but had a time lag of ~2.5 h at the end of the last upper-most FAAM leg. (c) PV at 325 K (shading) and MSLP (black contours, in hPa) at 12 UTC 23 Sep 2016 with HALO flight track from Iceland (gray / green line; green part corresponds to the section shown in (a) and (b)) and FAAM flight track (gray / black line; black part corresponds to track in (a) and (b)). The circle and diamond markers indicate the start and end positions of the latitudinal WCB cross-sections. (d) Ice water content as observed along the FAAM flight track. Differences between the flight tracks in (a/b) and (d) result from interpolation of FAAM position to the closest HALO observation in (a). The longitude axis in (d) was reversed to match with the HALO flight track.

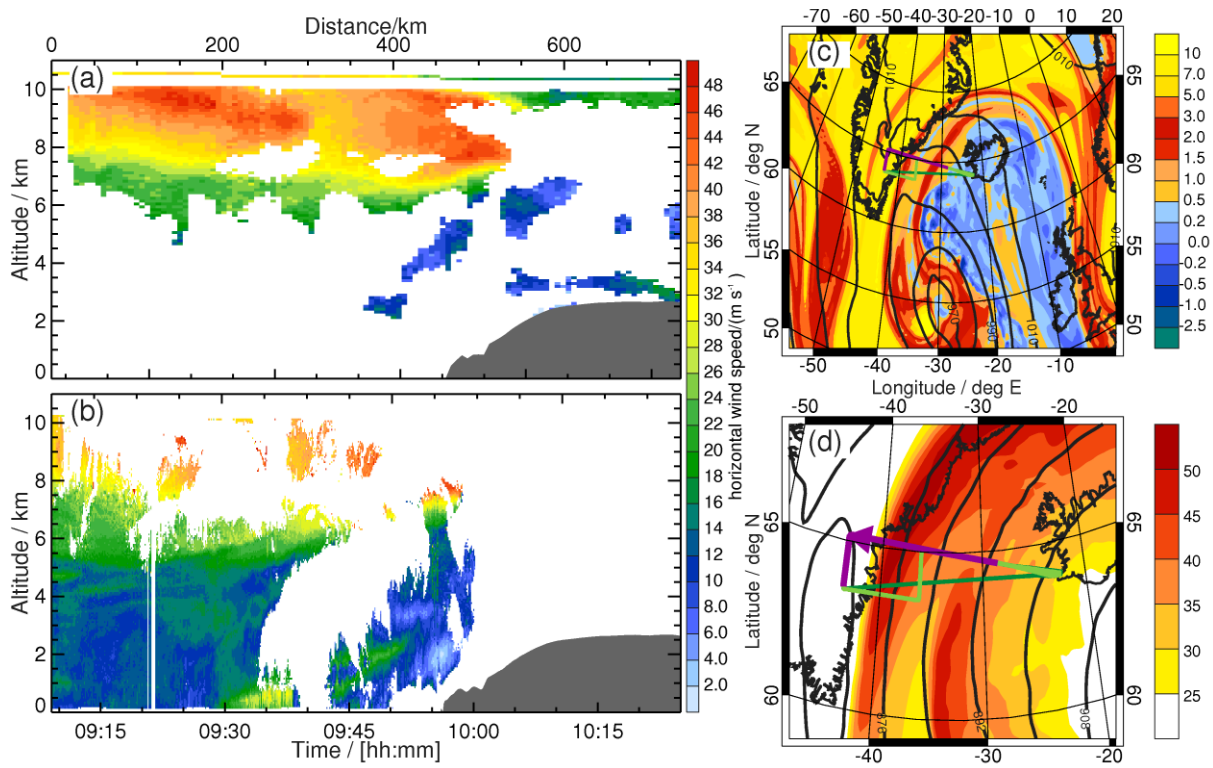

Fig. 9. Jet stream observations on 2 October 2016 (IOP6): (a) DLR Falcon 2-µm DWL wind speeds (colors) and (b) SAFIRE radar-derived wind speeds (colors). Grey area in (a) and (b) marks the topography of Greenland. (c) PV at 320 K (shading) and MSLP (black contours, in hPa), and (d) 300 hPa wind speed (colors) and geopotential height (black contours, in dam) at 06 UTC 2 Oct 2016. (c) and (d) include flight tracks of the DLR Falcon (light green line) and SAFIRE Falcon (dark green line). The coordinated part of the flight from east to west shown in (a) and (b) is marked with the purple line.

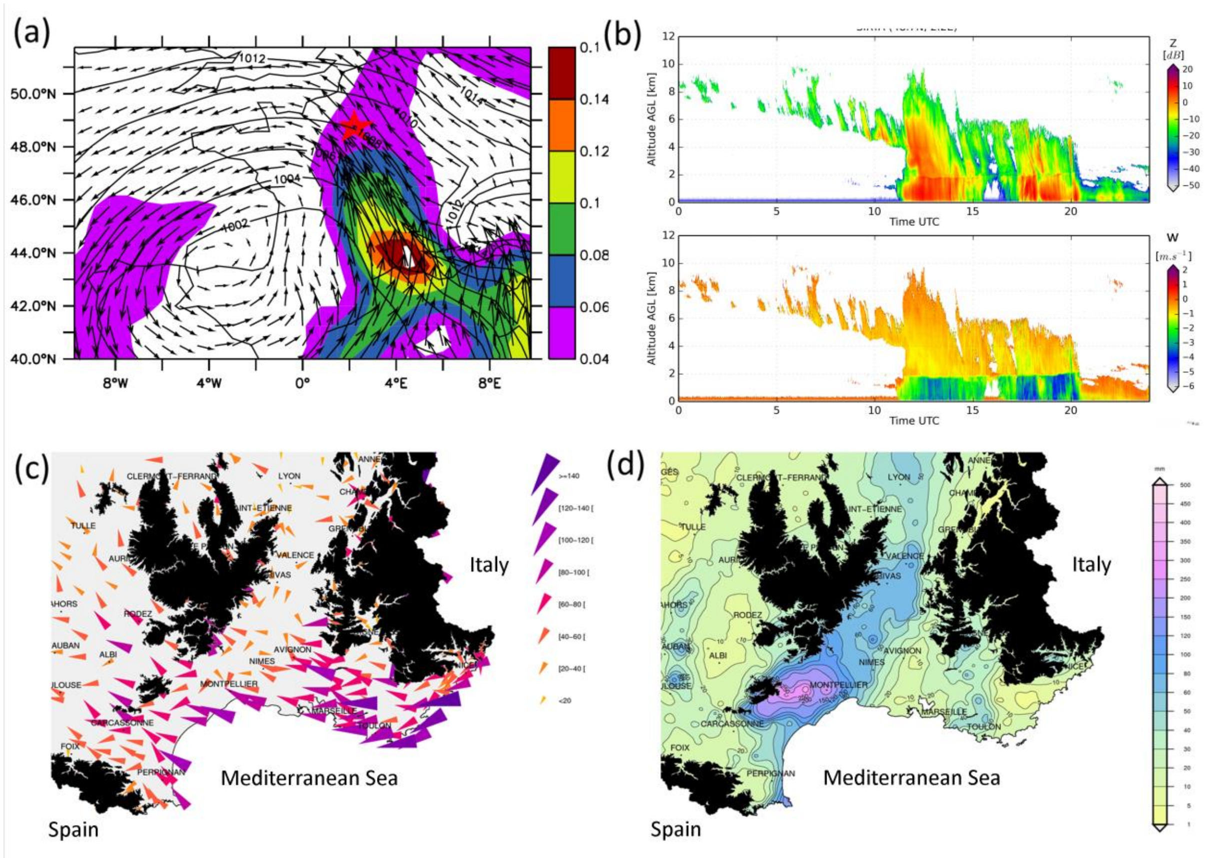

Fig.10. (a) ERA Interim moisture fluxes at 850 hPa (arrows, shadings shows magnitude) and surface pressure (black contours, hPa) at 12 UTC 13 Oct 2016. The red star indicates the location of the SIRTA surface observation site. (b) Reflectivity and Doppler velocity (approximately equal to terminal fall speed) at the 25m resolution of the radar BASTA at SIRTA on 13 Oct 2016. (c) Daily accumulated precipitation (mm) and (d) daily maximum of instantaneous surface wind in Southern France on 13 Oct 2016 from the high-resolution climatological network of Météo-France surface weather stations. The black areas in (c) and (d) mark topography of the French Pyrenees, the Massif Central and the French Alps.

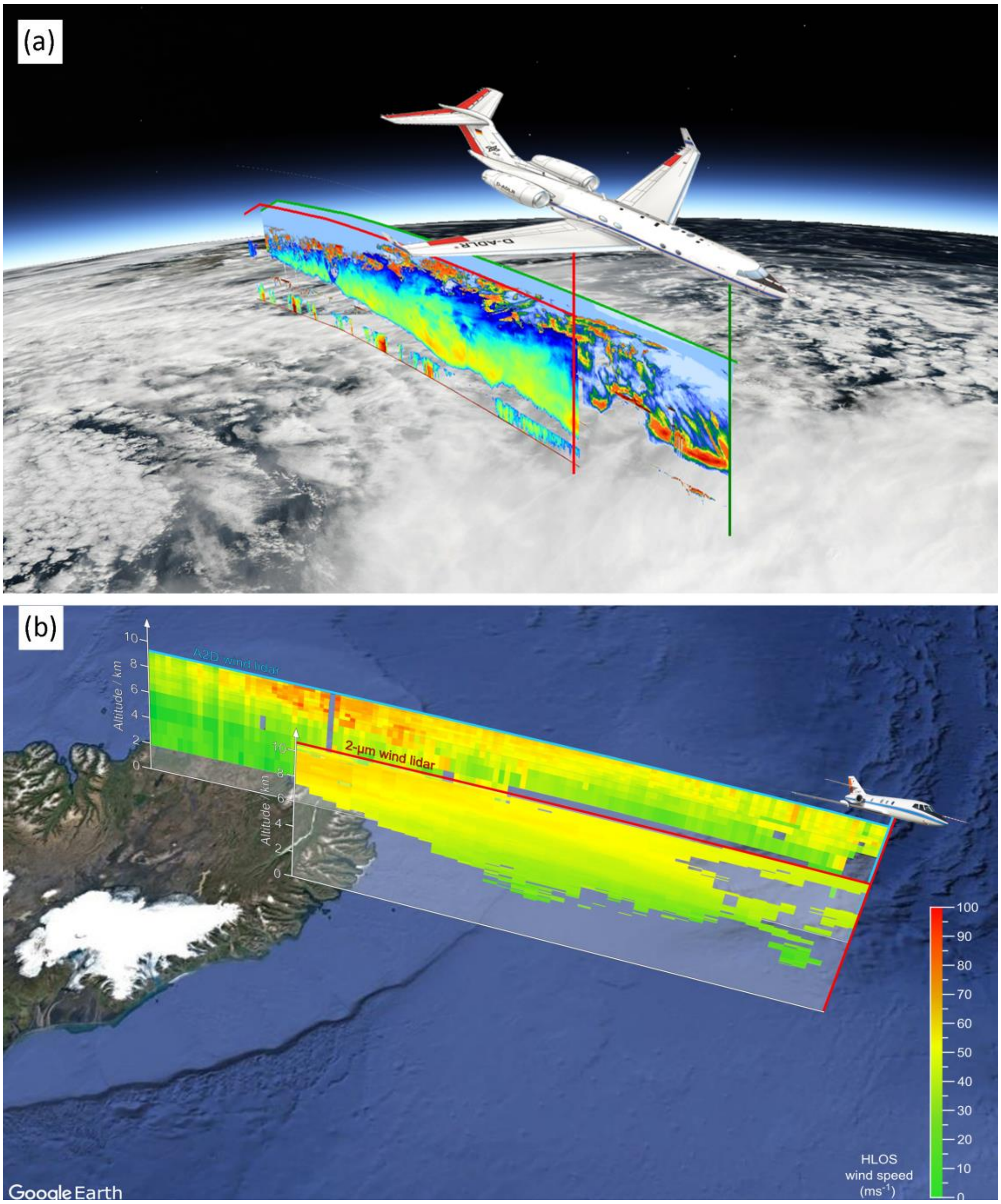

Fig. SB1. (a) Collocated observations of the vertical cloud structure below HALO, based on lidar (backscatter, along green part of the flight) and radar (radar reflectivity along red line). The underlying true color image was acquired by MODIS Aqua near the time of the flight (Global Imagery Browse Services (GIBS), operated by the NASA/GSFC/Earth Science Data and Information System). (b) Collocated wind observations on board the DLR Falcon using the A2D direct-detection wind lidar (along the blue line) and the 2-µm coherent DWL (along the red line). The latter is horizontally displaced from the actual flight track for clarity (Background picture: © 2017 Google).

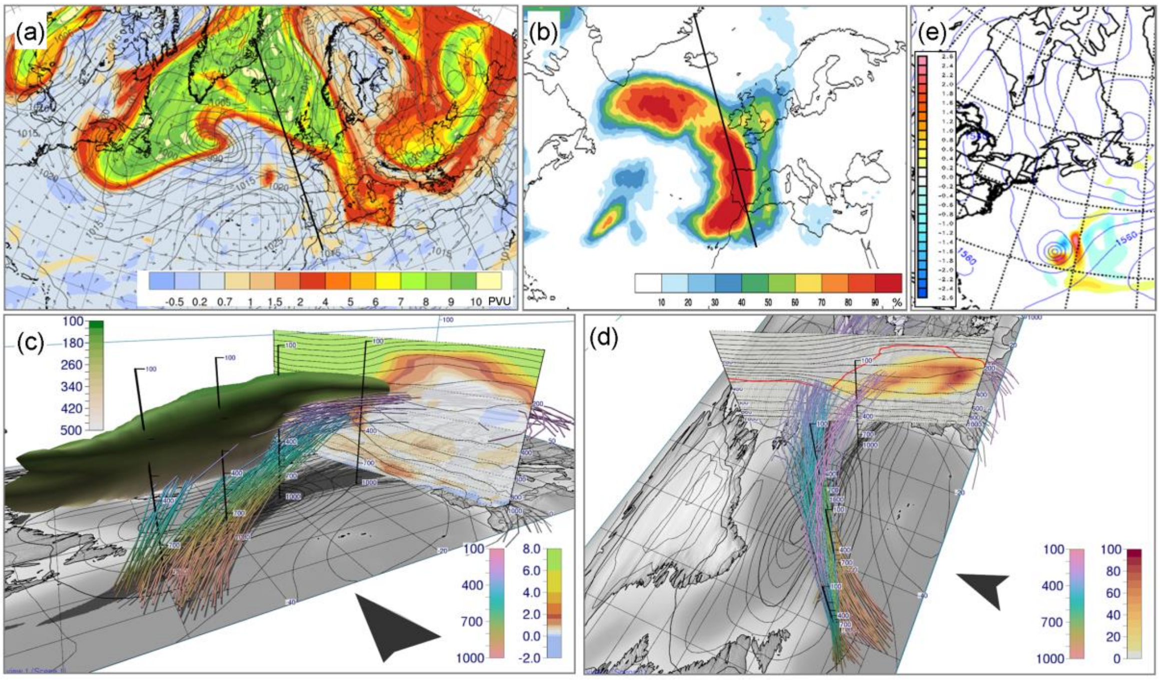

Fig. SB2. NAWDEX forecast products for 12 UTC 26 September 2016 (lead time +60 h): (a) ECMWF IFS deterministic forecast of PV on 330 K (color shading) and mean sea level pressure (MSLP, in hPa). (b) WCB column probabilities of occurrence (color shading in %), derived from ECMWF ensemble (Schäfler et al. 2014; Rautenhaus et al. 2015). Black line indicates location of cross section in Met.3D visualizations in (c) and (d). (c) Isosurface of ensemble mean wind of 60 m s^{-1} (color indicates pressure on isosurface in hPa) and MSLP (black surface contours). The cross section shows ensemble mean PV (color shading) and potential temperature (black contours). Colored lines represent WCB trajectories of ensemble member 22, starting at 06 UTC 25 September 2016 (colored by pressure). The black vertical poles have been added to aid spatial perception; they are labeled with pressure in hPa. (d) WCB trajectories as in (c) but from a different viewpoint and combined with a cross section showing 3D WCB probabilities (color shading, in %), ensemble mean potential temperature (black contours) and the 2 PVU isoline (red contour). (e) COAMPS adjoint 48 h forecast moisture sensitivity at 850 hPa [color shading, increments every 0.2 m^2 s^{-2} (g kg^{-1})$^{-1}$] and 850 hPa geopotential heights (contours every 30 m) valid at 12 UTC 24 September (initial forecast time).